Journal of Sound and Vibration 329 (2010) 2654–2682

Contents lists available at ScienceDirect

Journal of Sound and Vibration

journal homepage: www.elsevier.com/locate/jsvi

Uncertainty analysis of the standard delay-and-sum beamformer and array calibration

T. Yardibi [a], C. Bahr [b], N. Zawodny [b], F. Liu [b], L.N. Cattafesta III [b,*], J. Li [a]

[a] Department of Electrical and Computer Engineering, University of Florida, Gainesville, FL 32611, USA
[b] Department of Mechanical and Aerospace Engineering, University of Florida, Gainesville, FL 32611, USA

ARTICLE INFO

Article history:
Received 24 May 2009
Received in revised form
15 December 2009
Accepted 12 January 2010
Handling Editor: K. Shin
Available online 6 February 2010

ABSTRACT

Beamforming has become an ubiquitous task in aeroacoustic noise measurements for source localization and power estimation. The standard delay-and-sum (DAS) beamformer is the most commonly used beamforming algorithm due to its simplicity and robustness and also serves as the basis for more sophisticated algorithms, such as the deconvolution approach for the mapping of acoustic sources (DAMAS). The DAS data reduction equation is a function of many parameters including the microphone locations, microphone transfer functions, temperature and the cross-spectral matrix (CSM), where each one of these parameters has a unique uncertainty associated with it. This paper provides a systematic uncertainty analysis of the DAS beamformer and Dougherty's widely used calibration procedure under the assumption that the underlying mathematical model of incoherent, monopole sources is correct. An analytical multivariate method based on a first-order Taylor series expansion and a numerical Monte-Carlo method based on assumed uncertainty distributions for the input variables are considered. The uncertainty of calibration is analyzed using the Monte-Carlo method, whereas the uncertainty of the DAS beamformer is analyzed using both the complex multivariate and the Monte-Carlo methods. It is shown that the multivariate uncertainty analysis method fails when the perturbations are relatively large and/or the output distribution is non-Gaussian, and therefore the Monte-Carlo analysis should be used in the general case. The calibration procedure is shown to greatly reduce the uncertainties in the DAS power estimates. In particular, 95 percent confidence intervals for the DAS power estimates are presented with simulated data for various scenarios. Moreover, the 95 percent confidence intervals for the integrated DAS levels at different frequencies are computed using experimental data. It is shown that with experimental data, the 95 percent confidence intervals for the integrated power levels are within ± 1 dB of the mean levels when the component uncertainties are set at low but achievable values.

1. Introduction

The use of microphone arrays has become common practice in aeroacoustic testing in recent years. Beamforming algorithms are used to electronically steer a microphone array to desired regions in space for creating an image of acoustic sources at a given frequency. This image consists of the sound pressure levels of all the scanning points in the region of

* Corresponding author. Tel.: +1 352 846 3017; fax: +1 352 846 3028.
E-mail address: cattafes@ufl.edu (L.N. Cattafesta III).

0022-460X/$ - see front matter © 2010 Elsevier Ltd. All rights reserved.
doi:10.1016/j.jsv.2010.01.014

interest [1,2]. The most widely employed beamforming algorithm in practice is the delay-and-sum (DAS) beamformer [1–4], which sums the delayed and weighted versions of each microphone signal so that the actual source signals are reinforced and the unwanted noise signals tend to cancel. Alternative microphone array processing methods, such as the deconvolution approach for the mapping of acoustic sources (DAMAS) [5], variations of DAMAS including DAMAS2 [6] and sparsity constrained DAMAS (SC-DAMAS) [7,8], covariance matrix fitting (CMF) [7,8], and CLEAN based on source coherence (CLEAN-SC) [9], have been developed in order to mitigate the drawbacks of the DAS beamformer, such as low resolution and frequency-dependent response.

Although the DAS beamformer has been used in many aeroacoustic noise localization studies, a systematic analysis of its uncertainty is not available to the best of the authors' knowledge. The purpose of this paper, therefore, is to provide a detailed uncertainty analysis of the DAS beamformer [1,2] and the popular calibration procedure introduced by Dougherty [2]. Calibration is applied to account for the errors in the assumed steering vectors and basically consists of measuring the acoustic free field produced by a single speaker driven by broadband noise in the absence of flow. The eigen-decomposition of the cross-spectral matrix (CSM) is used to obtain frequency-dependent and complex microphone correction factors for the assumed dominant monopole output of the speaker. These correction factors are then embedded in the DAS data reduction equation for better performance.

Uncertainty analysis answers the question of how good the results of an experiment are and, without such an analysis, it is difficult to state the confidence in the obtained estimates [10]. A standard method to calculate the output uncertainties is to propagate the uncertainties of the input variables through the data reduction equation (the equation used to estimate the quantities of interest from the measurements). The data reduction equation is a function of multiple input variables, most of which are obtained from separate measurements. Note that the uncertainties of the input variables are not necessarily uncorrelated. For instance, the DAS data reduction equation contains both real- and complex-valued input variables and, in general, the real and imaginary components of the complex-valued components are correlated. As will be shown below, this leads to increased complexity in the uncertainty analysis.

Both complex multivariate and Monte-Carlo uncertainty analysis will be considered in this paper. The multivariate analysis is based on a first-order Taylor series expansion of the quantities of interest and assumes that the perturbations are relatively small, and hence, the nonlinear terms in the Taylor series expansion are negligible. It also assumes that the output distributions are Gaussian in order to compute the confidence intervals. The multivariate uncertainty analysis differs from the classical uncertainty techniques in that it estimates the correlation of the output variables [11]. The Monte-Carlo method, on the other hand, uses assumed distributions for the input variables, which may be correlated. Random perturbations for the input variables are drawn from these distributions and the data reduction equation is evaluated using the perturbed input variables. This process is repeated until the distributions of the output variables have converged, after which the uncertainty estimate can be readily obtained from these distributions. The advantage of the multivariate analysis is that it is analytical and can estimate the uncertainties relatively quickly. However, more often than not, closed-form expressions for the derivatives involved in the Taylor series expansion are not available or very cumbersome, and the input perturbations are not small enough to assume linearity. In addition, the Gaussian-type assumptions made when estimating the confidence intervals from the sample covariance matrices might be violated in practice. Monte-Carlo analysis provides much more flexibility in terms of designing the experiments since the data reduction equation is already implemented for the experimental analysis and embedding the perturbations of the input variables to this equation is in general straightforward.

Castellini et al. [12] study the uncertainty of the DAS beamformer for a 2D linear array and far-field noise propagation where the source locations are parameterized by angles ranging from 0 to π rather than being parameterized by 3D locations. Moreover, the analysis provided is not targeted directly for aeroacoustic applications and does not consider the uncertainties in the CSM, calibration or integrated DAS sound pressure levels (SPL). In this paper, we specifically analyze the uncertainty of the DAS beamformer as implemented in aeroacoustic measurements [1–3,5].

The remainder of this paper is organized as follows. First, the data model assumed throughout the paper is introduced, and the DAS beamformer and the calibration procedure is outlined. General descriptions of the multivariate uncertainty analysis as well as the Monte-Carlo uncertainty analysis follow. Next, the equations needed for the application of these two methods to the DAS beamformer are derived, after which the numerical and experimental results are provided. The numerical examples start with the Monte-Carlo uncertainty analysis of the calibration procedure. Following this analysis, the multivariate and Monte-Carlo uncertainty analyses of the DAS beamformer are presented. The paper concludes with the uncertainty analysis of the integrated DAS levels using experimental data acquired at the University of Florida Aeroacoustic Flow Facility (UFAFF) [13].

In the following, vectors and matrices are denoted by boldface lowercase and boldface uppercase letters, respectively. Other mathematical symbols are defined after their first appearances. All sound pressure levels presented in this paper are in dB re. 20 μPa.

2. Beamforming in aeroacoustic measurements

In this section we introduce the traditional data model used in aeroacoustic measurement applications, and describe the standard DAS beamforming algorithm and the array calibration procedure [2].

2.1. Data model

Consider the wave field generated by L incoherent monopole acoustic sources where the 3D location of the l th source is denoted by $(\tilde{x}_l, \tilde{y}_l, \tilde{z}_l)$ for $l=1,\ldots,L$. The data reduction process for frequency domain beamforming starts with the computation of the CSM at each frequency of interest. For this purpose, the pressure data recorded at each microphone for T_{acq} seconds is divided into ν percent overlapping blocks of length H, where $0 \le \nu < 100$. The resulting number of blocks, B, can be computed as follows:

$$B = \left\lfloor 1 + \frac{T_{\mathrm{acq}} f_s/H - 1}{1-\nu/100} \right\rfloor, \tag{1}$$

where $\lfloor\cdot\rfloor$ denotes the nearest integer less than or equal to the argument and f_s denotes the sampling frequency. Next, the H-point fast Fourier transform (FFT) of each block is computed (an appropriate spectral window can be applied to the data before taking the Fourier transforms), where H is a power of 2. This results in a frequency resolution of f_s/H. The h th element of each frequency domain block corresponds to the narrow-band frequency $f_h = hf_s/H$, where $h=0,\ldots,H/2$ and only the single-sided spectrum is considered.

Consider an M-element microphone array with the m th microphone located at (x_m, y_m, z_m), where $m=1,\ldots,M$. Let the frequency of interest be f. Following the spherical wave propagation model [14], the frequency domain pressure data at all the microphones can be used to obtain the following set of equations [15]:

$$\mathbf{y}(b) = \sum_{l=1}^{L} \mathbf{a}_l s_l(b) + \mathbf{e}(b), \quad b=1,\ldots,B, \tag{2}$$

where

$$\mathbf{y}(b) = \begin{bmatrix} y_1(b) \\ y_2(b) \\ \vdots \\ y_M(b) \end{bmatrix}, \quad \mathbf{a}_l = \begin{bmatrix} \mathrm{e}^{-\mathrm{j}kr_{l,1}}/r_{l,1} \\ \mathrm{e}^{-\mathrm{j}kr_{l,2}}/r_{l,2} \\ \vdots \\ \mathrm{e}^{-\mathrm{j}kr_{l,M}}/r_{l,M} \end{bmatrix}, \quad \mathbf{e}(b) = \begin{bmatrix} e_1(b) \\ e_2(b) \\ \vdots \\ e_M(b) \end{bmatrix}, \tag{3}$$

$y_m(b)$ is the frequency domain pressure data of microphone m at block b, $\mathbf{a}_l$ is the steering vector (or the wave propagation vector) corresponding to the l th monopole source, $r_{l,m} = \sqrt{(\tilde{x}_l - x_m)^2 + (\tilde{y}_l - y_m)^2 + (\tilde{z}_l - z_m)^2}$ is the Euclidean distance between the l th source and the m th microphone, $k = 2\pi f/c$ is the wavenumber, c is the speed of sound in air, $s_l(b)$ is the acoustic waveform of the l th source at block b, and $e_m(b)$ is the additive contamination noise (due to electronic noise and acoustic sources other than the L sources considered as well as reflections and scattering) at the m th microphone at block b. Note that $\mathbf{y}(b)$, $\mathbf{a}_l$ and $\mathbf{e}(b)$ are all complex vectors of size $M \times 1$, and $s_l(b)$ is a complex scalar. In addition, $\mathbf{y}(b)$ and $\mathbf{a}_l$ are known, whereas $s_l(b)$ and $\mathbf{e}(b)$ are unknown quantities. Note also that the indices l, m and b run from 1 to L, M and B, respectively.

2.2. DAS beamformer

The DAS beamformer basically sums the delayed and weighted versions of each microphone signal in order to reinforce the signal from the source of interest while suppressing the contribution from other sources and contamination noise. The delays and weights are designed according to the relative distances between the microphones. In the frequency domain, this corresponds to applying appropriate phase shifts and weighting factors. Beamforming is usually done independently at each narrow-band frequency of interest and therefore in the following analysis, we will consider only one particular frequency f (the same analysis is repeated at all frequencies of interest). The DAS estimate of the l th source is defined as [1,5]

$$\tilde{s}_l(b) = \frac{1}{M} \tilde{\mathbf{a}}_l^{\mathrm{H}} \mathbf{y}(b), \quad l=1,\ldots,L, \tag{4}$$

where

$$\tilde{\mathbf{a}}_l = \frac{1}{r_{l,0}} [r_{l,1}\mathrm{e}^{-\mathrm{j}kr_{l,1}}, r_{l,2}\mathrm{e}^{-\mathrm{j}kr_{l,2}}, \ldots, r_{l,M}\mathrm{e}^{-\mathrm{j}kr_{l,M}}]^{\mathrm{T}}, \tag{5}$$

$r_{l,0} = \sqrt{(\tilde{x}_l - \overline{x})^2 + (\tilde{y}_l - \overline{y})^2 + (\tilde{z}_l - \overline{z})^2}$ is the distance from the l th scanning point to the array center, $\overline{x}$ is the x component of the array center ($\overline{y}$ and $\overline{z}$ are defined similarly), and $(\cdot)^{\mathrm{T}}$ and $(\cdot)^{\mathrm{H}}$ denote the transpose and conjugate transpose of the argument, respectively. Note that $\tilde{\mathbf{a}}_l$, which is an $M \times 1$ complex vector that is known, is used to account for the different distances traveled by the wave before reaching each microphone. The purpose of normalizing $\tilde{\mathbf{a}}_l$ by $r_{l,0}$ is to match the estimated signal power to what a single microphone in the center of the array would measure. The underlying assumption behind DAS is that while $r_{l,0}\tilde{\mathbf{a}}_l^{\mathrm{H}}\mathbf{a}_l = M$, $r_{l',0}\tilde{\mathbf{a}}_{l'}^{\mathrm{H}}\mathbf{a}_l$ is relatively small for $l' \neq l$, $l,l' = 1,\ldots,L$. This assumption is evaluated by analyzing the so-called point spread function, psf(l), defined as $|\tilde{\mathbf{a}}_l^{\mathrm{H}}\mathbf{a}_0|/M^2$ for the l th scanning point where $\mathbf{a}_0$ denotes the wave

propagation vector of a source located at the center of the scanning region. The psf is also used to compute the 3-dB beamwidth (and the resolution) of the array.

Consequently, DAS estimates the power level of the l th source (as measured at the array center) as follows:

$$P_l = \frac{2}{\omega_0 B}\sum_{b=1}^{B}|\tilde{s}_l(b)|^2 = \frac{1}{M^2}\tilde{\mathbf{a}}_l^{\mathrm{H}}\mathbf{G}\tilde{\mathbf{a}}_l, \quad l=1,\ldots,L, \tag{6}$$

where ω_0 is the spectral window correction factor and

$$\mathbf{G} = \frac{2}{\omega_0 B}\sum_{b=1}^{B}\mathbf{y}(b)\mathbf{y}^{\mathrm{H}}(b) \tag{7}$$

is the CSM. (The factor of 2 is due to the use of the single-sided spectrum.) The CSM is an $M\times M$ complex symmetric matrix and hence consists of M^2 real-valued distinct components. In general, it is preferable to work with the CSM, $\mathbf{G}$, and Eq. (6) rather than the frequency domain pressure data, $\mathbf{y}(b)$, and Eq. (4) as the CSMs require much less storage space and are more convenient for analysis.

The number of sources, L, is unknown beforehand and hence L is considered to be the number of scanning points in the region. In other words, every point of a predefined grid that covers the region of interest is considered as a potential source whose corresponding sound pressure level at the array center will be estimated.

In general, each of the array microphones do not possess flat frequency response with zero phase, and this is accounted for via a frequency-dependent $M\times M$ diagonal calibration matrix $\tilde{\mathbf{D}} = \mathrm{diag}(\tilde{D}_1,\ldots,\tilde{D}_M)$, where $\tilde{D}_m$ denotes the complex correction factor for microphone m. The calibrated DAS data reduction equation then becomes

$$P_l = \frac{1}{M^2}\tilde{\mathbf{a}}_l^{\mathrm{H}}\tilde{\mathbf{D}}\mathbf{G}\tilde{\mathbf{D}}^{\mathrm{H}}\tilde{\mathbf{a}}_l, \quad l=1,\ldots,L. \tag{8}$$

Note that if a microphone is known to be problematic, simply placing a 0 in the corresponding diagonal entry of $\tilde{\mathbf{D}}$ and changing M to $M-1$ will prevent it from propagating through the data reduction equation. The next subsection describes how $\tilde{\mathbf{D}}$ can be obtained in practice.

2.3. Array calibration

In order for DAS to give accurate source location and strength estimates, the assumed steering vectors have to be close to the true ones. Errors in microphone locations and temperature (through its effect on the sound speed) can have major effects on the DAS signal power estimates, especially at relatively high frequencies, since these errors are multiplied by the wavenumber before propagating through the DAS data reduction equation. This section describes a widely used calibration procedure introduced by Dougherty [2] to remedy this problem. The calibration setup consists of a speaker that resembles a point source and is driven with a broadband signal (or a tonal signal where the tone frequency is varied). The speaker is placed near the model location and a temporary anechoic enclosure is recommended for a hardwall wind tunnel to minimize source reflections [2]. Array data is collected with no flow and the resulting CSM is analyzed at each frequency to obtain frequency-dependent complex correction factors for all the microphones.

Theoretically, the measurements in the presence of a single source are modeled as (see Eq. (2))

$$\mathbf{y}(b) = \mathbf{a}_{\mathrm{cal}}s_{\mathrm{cal}}(b), \quad b=1,\ldots,B, \tag{9}$$

where $\mathbf{a}_{\mathrm{cal}}$ is the *actual* steering vector (unknown) corresponding to the location of the calibration speaker, $s_{\mathrm{cal}}(b)$ is the calibration speaker waveform (unknown) and the noise term $\mathbf{e}(b)$ is neglected. According to Eq. (7), the CSM becomes

$$\mathbf{G}_{\mathrm{cal}} = P_{\mathrm{cal}}\mathbf{a}_{\mathrm{cal}}\mathbf{a}_{\mathrm{cal}}^{\mathrm{H}}, \tag{10}$$

where P_{cal} is the signal power of the calibration speaker. Since $\mathbf{G}_{\mathrm{cal}}$ is an outer product (and hence rank-1), it has only a single non-zero eigenvector equal to $\boldsymbol{\lambda}_{\mathrm{cal}} = \mathbf{a}_{\mathrm{cal}}\mathrm{e}^{\mathrm{j}\phi}/\|\mathbf{a}_{\mathrm{cal}}\|$ and a single non-zero eigenvalue equal to $\nu_{\mathrm{cal}} = P_{\mathrm{cal}}\|\mathbf{a}_{\mathrm{cal}}\|^2$, where $0\le\phi\le 2\pi$ is an arbitrary phase value and $\|\cdot\|$ denotes the Euclidean norm. In practice, although the remaining eigenvalues will not be identically zero, the dominant eigenvalue is expected to be noticeably larger with a good quality speaker that produces sufficient sound [2]. The measurement of the m th microphone is then scaled by the complex coefficient

$$\tilde{D}_m = \frac{(\boldsymbol{\lambda}_{\mathrm{theory}})_m}{(\boldsymbol{\lambda}_{\mathrm{cal}})_m}, \quad m=1,\ldots,M, \tag{11}$$

where $(\cdot)_m$ denotes the m th element of the vector argument, $\boldsymbol{\lambda}_{\mathrm{theory}} = \mathbf{a}_{\mathrm{theory}}/\|\mathbf{a}_{\mathrm{theory}}\|$, and $\mathbf{a}_{\mathrm{theory}}$ is given by Eq. (3) where $r_{l,m}$ is replaced by the distance between the calibration speaker and the m th microphone. It is assumed that $\|\mathbf{a}_{\mathrm{cal}}\|\approx\|\mathbf{a}_{\mathrm{theory}}\|$ and therefore

$$\mathbf{y}_{\mathrm{calibrated}}(b) = \tilde{\mathbf{D}}\mathbf{y}(b) = \frac{\|\mathbf{a}_{\mathrm{cal}}\|\mathrm{e}^{-\mathrm{j}\phi}}{\|\mathbf{a}_{\mathrm{theory}}\|}\mathbf{a}_{\mathrm{theory}}s_{\mathrm{cal}}(b) \approx \mathrm{e}^{-\mathrm{j}\phi}\mathbf{a}_{\mathrm{theory}}s_{\mathrm{cal}}(b), \quad b=1,\ldots,B. \tag{12}$$

The constant phase offset $\mathrm{e}^{-\mathrm{j}\phi}$ will disappear when the power levels are considered. The reason for the normalization $\|\mathbf{a}_{\mathrm{cal}}\|/\|\mathbf{a}_{\mathrm{theory}}\|$ is because only ν_{cal} is known in practice and not $\mathbf{a}_{\mathrm{cal}}$ or $\|\mathbf{a}_{\mathrm{cal}}\|$ (i.e., there is a scaling ambiguity). An important

aspect of the calibration is that it will correct the phase mismatch perfectly for the calibration data. As the distance between the beamforming source (during testing) and the calibration speaker locations increase, the benefit of calibration is expected to degrade [2].

The calibration procedure described above corrects the frequency response differences between the microphones. An additional step can be employed where an overall array correction factor is obtained with respect to a reference microphone that is assumed to be calibrated separately. Note that the dominant eigenvalue of the calibrated CSM, $\tilde{\mathbf{D}}\mathbf{G}_{\mathrm{cal}}\tilde{\mathbf{D}}^{\mathrm{H}}$, is approximately $\nu = P_{\mathrm{cal}}M/r_c^2$, where r_c is the distance from the calibration speaker to the array center, and the reference microphone will measure $P_{\mathrm{ref}} = P_{\mathrm{cal}}/r_{\mathrm{ref}}^2$, where r_{ref} is the distance from the calibration speaker to the reference microphone. The overall array correction factor is then given as

$$P_{\mathrm{ref}}\left(\frac{r_{\mathrm{ref}}}{r_c}\right)^2\frac{M}{\nu}. \tag{13}$$

When all the assumptions mentioned above are met, calibration will provide accurate correction factors for a source near the calibration speaker location. However, in practice, many sources of uncertainty are present during calibration. Errors in CSM and reference microphone levels are two such uncertainty sources. In addition, it might be easier to measure the distance between the calibration speaker and the array than it is to measure the distance between a complex test model and the array. This will cause uncertainties in the array broadband distance, which is the distance from the array center to the center of the scanning region, for which calibration cannot account. We will consider these uncertainties in the numerical examples section. The calibration performance will also degrade when the calibration source is not a perfect monopole and/or there are reflections in the calibration setup. However, in this paper, we do not consider such modeling errors and instead focus our attention on the uncertainty of the calibration procedure when the underlying data model is correct. (Similarly, when evaluating the uncertainty of the DAS beamformer, the data model is assumed to be correct.)

3. Uncertainty analysis

In experimental data analysis, the goal is to estimate one or more quantities of interest using a data reduction equation. The data reduction equation is in general a function of many input variables, most of which are obtained from some other measurements themselves. One purpose of uncertainty analysis is to propagate the uncertainties of all the input variables through the data reduction equation in order to estimate the total effect on the estimation performance. Another purpose is to understand the dominant sources of uncertainty and how the errors scale [10]. Experimental data analysis should provide not only the estimates of the quantities of interest but also the uncertainties associated with these estimated values since without an uncertainty analysis, it is difficult to understand how accurate the results really are.

As mentioned in Section 1, we consider two uncertainty analysis techniques in this paper: (i) multivariate uncertainty analysis, which is based on a first-order Taylor series expansion and (ii) Monte-Carlo uncertainty analysis, which is based on assuming distributions for each input variable. We apply both multivariate and Monte-Carlo uncertainty analyses to the DAS beamformer, whereas we apply Monte-Carlo uncertainty analysis to calibration (due to the complexity of the nonlinear eigen-decomposition involved in the procedure). The following analyses consider only a single beamforming location (in particular, the l th one) and should be repeated for every point in the scanning grid, i.e., L times.

3.1. Multivariate uncertainty analysis

The classical uncertainty analysis technique estimates the uncertainty of the output variables by making use of a first-order Taylor series expansion. The uncertainties of the input variables should be sufficiently small so that the linear approximation remains valid. The resulting sample standard deviation or the standard uncertainty of a variable, P_l in our case (see Eq. (8)), is then computed by

$$g_{P_l} = \sqrt{\sum_{t=1}^{T'}\left(\frac{\partial P_l}{\partial V_t}\right)^2 \Gamma_{V_t,V_t} + 2\sum_{t=1}^{T'-1}\sum_{u=t+1}^{T'}\frac{\partial P_l}{\partial V_t}\frac{\partial P_l}{\partial V_u}\Gamma_{V_t,V_u}}, \tag{14}$$

where T' is the number of input variables, Γ_{V_t,V_t} is the standard uncertainty squared of the t th input variable, $\partial P/\partial V_t$ is called the sensitivity coefficient of the t th input variable, and Γ_{V_t,V_u} is the sample covariance between the t th and u th input variables. Note that t and u run from 1 to T' and $t+1$ to T', respectively.

In the DAS data reduction equation, the power estimate P_l is real-valued and the input variables are complex-valued. However, Eq. (14) is derived for real variables and therefore the complex input variables should be separated into their real and imaginary components before being propagated through the data reduction equation [16–18]. One important reason for treating the real and imaginary parts of the input variables separately is because these components can be correlated in many applications. (Note that the second term in the square root in Eq. (14) accounts for the correlation between such components.) For the DAS beamformer, since only one real-valued power level is considered at a time, the multivariate and classical uncertainty analysis methods are similar [18].

Eq. (14) can also be written in matrix form as follows [16–18]:

$$g_{P_l} = \sqrt{\mathbf{J}\boldsymbol{\Gamma}\mathbf{J}^{\mathrm{T}}}, \tag{15}$$

where $\boldsymbol{\Gamma}$ is the $2T' \times 2T'$ real-valued and symmetric sample covariance matrix of the real and imaginary parts of all the input variables, i.e., the variables $\{\mathrm{Re}\{V_1\},\ldots,\mathrm{Re}\{V_{T'}\},\mathrm{Im}\{V_1\},\ldots,\mathrm{Im}\{V_{T'}\}\}$ with $\mathrm{Re}\{\cdot\}$ and $\mathrm{Im}\{\cdot\}$ denoting the real and imaginary parts of the argument, respectively, and $\mathbf{J}$ is the $1 \times 2T'$ real-valued Jacobian matrix (a vector in our case) defined as

$$\mathbf{J} = \left[\frac{\partial P_l}{\partial \mathrm{Re}\{V_1\}},\ldots,\frac{\partial P_l}{\partial \mathrm{Re}\{V_{T'}\}},\frac{\partial P_l}{\partial \mathrm{Im}\{V_1\}},\ldots,\frac{\partial P_l}{\partial \mathrm{Im}\{V_{T'}\}}\right]. \tag{16}$$

Consider a simple example with two real variables, V_1 and V_2, where V_1 and V_2 are assumed to be uncorrelated and let the output variable P_l be a function of V_1 and V_2. Then Eq. (14) or (15) becomes

$$g_{P_l} = \sqrt{\begin{bmatrix}\frac{\partial P_l}{\partial V_1} & \frac{\partial P_l}{\partial V_2}\end{bmatrix}\begin{bmatrix}\Gamma_{V_1,V_1} & 0\\ 0 & \Gamma_{V_2,V_2}\end{bmatrix}\begin{bmatrix}\frac{\partial P_l}{\partial V_1}\\ \frac{\partial P_l}{\partial V_2}\end{bmatrix}} = \sqrt{\left(\frac{\partial P_l}{\partial V_1}\right)^2\Gamma_{V_1,V_1} + \left(\frac{\partial P_l}{\partial V_2}\right)^2\Gamma_{V_2,V_2}}, \tag{17}$$

where the squared uncertainties of the variables V_1 and V_2 are scaled by the sensitivity coefficients $\partial P_l/\partial V_1$ and $\partial P_l/\partial V_2$ squared, respectively, and summed up to generate the final uncertainty squared.

In general, 95 percent confidence intervals are used when reporting the uncertainty results. In order to obtain the confidence intervals, g_{P_l} should be multiplied by a coverage factor which is simply taken as 2 in our case assuming a Gaussian distribution for the univariate output variable [18]. (Note that $(P_l-\overline{P}_l)/S_{P_l}$, where $\overline{P}_l$ and S_{P_l} are the sample mean and sample standard deviation of P_l, respectively, follows the t distribution with number of Monte-Carlo trials minus one degree of freedom. It is recommended that a coverage factor of 2 is used when the degrees of freedom is larger than 31 [10].)

3.2. Monte-Carlo uncertainty analysis

When the perturbations are relatively large (so that the linear assumption of the multivariate analysis is violated) and/or the output distributions are non-Gaussian, the multivariate method can no longer yield reliable uncertainty estimates. In addition, the sensitivity coefficients are often difficult to evaluate in closed-form. Therefore, a Monte-Carlo uncertainty analysis is preferable. In Monte-Carlo uncertainty analysis, a distribution is assumed for all of the input variables and then each variable is randomly perturbed using a perturbation value drawn from its uncertainty distribution (note that the input variables are not necessarily uncorrelated) [10,18]. Next, the perturbed input variables are propagated through the data reduction equation in order to obtain the perturbed output. This process is repeated until the distribution of the output variables converge [11]. The resulting distribution is then used to obtain the mean, variance (covariance) and 95 percent confidence intervals for the quantities of interest.

4. Application of uncertainty analysis to the DAS beamformer

In this section we describe how the aforementioned uncertainty analysis techniques can be applied to the DAS data reduction equation given in Eq. (8). Let

$$\mathbf{G} = \begin{bmatrix} G_{11} & C_{12}+jQ_{12} & \ldots & C_{1M}+jQ_{1M}\\ C_{12}-jQ_{12} & G_{22} & \ldots & C_{2M}+jQ_{2M}\\ \vdots & \vdots & \ddots & \vdots\\ C_{1M}-jQ_{1M} & C_{2M}-jQ_{2M} & \ldots & G_{MM}\end{bmatrix}, \tag{18}$$

where $C_{mn} = \mathrm{Re}\{G_{mn}\}$ and $Q_{mn} = \mathrm{Im}\{G_{mn}\}$, $m \neq n$, $m,n = 1,\ldots,M$. Similarly, let

$$\tilde{\mathbf{D}} = \begin{bmatrix} D_1+jE_1 & 0 & \ldots & 0\\ 0 & D_2+jE_2 & \ldots & 0\\ \vdots & \vdots & \ddots & \vdots\\ 0 & 0 & \ldots & D_M+jE_M\end{bmatrix}, \tag{19}$$

where $\tilde{D}_m = D_m + jE_m$, $D_m = \mathrm{Re}\{\tilde{D}_m\}$ and $E_m = \mathrm{Im}\{\tilde{D}_m\}$, $m = 1,\ldots,M$.

The input variables contained in Eq. (8) can be expressed as

$$\mathbf{V} = [\mathbf{V}_{\mathrm{CSM}}, \mathbf{V}_{\mathrm{Calib}}, \mathbf{V}_{\mathrm{Locs}}, V_{\mathrm{Temp}}], \tag{20}$$

where

$$\mathbf{V}_{\mathrm{CSM}} = [G_{11}, \ldots, G_{MM}, C_{12}, \ldots, C_{1M}, C_{23}, \ldots, C_{M-1,M}, Q_{12}, \ldots, Q_{1M}, Q_{23}, \ldots, Q_{M-1,M}], \tag{21}$$

$$\mathbf{V}_{\mathrm{Calib}} = [D_1, \ldots, D_M, E_1, \ldots, E_M], \tag{22}$$

$$\mathbf{V}_{\mathrm{Locs}} = [x_1, \ldots, x_M, y_1, \ldots, y_M, z_1, \ldots, z_M], \tag{23}$$

and, finally,

$$V_{\mathrm{Temp}} = [T]. \tag{24}$$

Table 1 lists the four categories of input variables as considered above.

The Jacobian matrix for P_l is defined as (see Eq. (16))

$$\mathbf{J} = \Bigg[\underbrace{\frac{\partial P_l}{\partial G_{11}}, \ldots, \frac{\partial P_l}{\partial Q_{M-1,M}}}_{\mathbf{J}_{\mathrm{CSM}}}, \underbrace{\frac{\partial P_l}{\partial D_1}, \ldots, \frac{\partial P_l}{\partial E_M}}_{\mathbf{J}_{\mathrm{Calib}}}, \underbrace{\frac{\partial P_l}{\partial x_1}, \ldots, \frac{\partial P_l}{\partial z_M}}_{\mathbf{J}_{\mathrm{Locs}}}, \underbrace{\frac{\partial P_l}{\partial T}}_{J_{\mathrm{Temp}}} \Bigg] \tag{25}$$

and therefore the 95 percent confidence interval for P_l is given by (see Eq. (15))

$$2g_{P_l} = 2(\mathbf{J}\mathbf{g}_{(\mathrm{CSM,Calib,Locs,Temp})}\mathbf{J}^{\mathrm{T}})^{1/2} = 2\left(\mathbf{J}_{\mathrm{CSM}}\mathbf{g}_{\mathrm{CSM}}\mathbf{J}_{\mathrm{CSM}}^{\mathrm{T}} + \mathbf{J}_{\mathrm{Calib}}\mathbf{g}_{\mathrm{Calib}}\mathbf{J}_{\mathrm{Calib}}^{\mathrm{T}} + \mathbf{J}_{\mathrm{Locs}}\mathbf{g}_{\mathrm{Locs}}\mathbf{J}_{\mathrm{Locs}}^{\mathrm{T}} + J_{\mathrm{Temp}}g_{\mathrm{Temp}}J_{\mathrm{Temp}}^{\mathrm{T}}\right)^{1/2}, \tag{26}$$

where $\mathbf{g}_{(\mathrm{CSM,Calib,Locs,Temp})}$ is the sample covariance matrix of $\mathbf{V}$ and $\mathbf{g}_{\mathrm{CSM}}$ is the sample covariance matrix of $\mathbf{V}_{\mathrm{CSM}}$ ($\mathbf{g}_{\mathrm{Calib}}$, $\mathbf{g}_{\mathrm{Locs}}$ and g_{Temp} are defined in a similar manner). (It is assumed that the CSM, calibration, microphone location and temperature errors are independent of each other.)

In order to evaluate Eq. (26), we need to compute the sample covariance matrices of the input variables, $\mathbf{g}_{\mathrm{CSM}}$, $\mathbf{g}_{\mathrm{Calib}}$, $\mathbf{g}_{\mathrm{Locs}}$, and g_{Temp}, as well as the Jacobian matrices, $\mathbf{J}_{\mathrm{CSM}}$, $\mathbf{J}_{\mathrm{Calib}}$, $\mathbf{J}_{\mathrm{Locs}}$ and J_{Temp}. We need the sample covariance matrices also for the Monte-Carlo analysis, since these will be the covariance matrices of the Gaussian distributions from which the random perturbations are drawn. The Jacobian matrices for each category of input variables, i.e., the terms in Eq. (25), are derived in Appendix A. When computing $\mathbf{g}_{\mathrm{CSM}}$, we consider the random errors associated with using the finite averaging method in Eq. (7). The expression for each component of $\mathbf{g}_{\mathrm{CSM}}$ is given in Table 9.1 of Bendat and Piersol [19] for two microphones (M=2). We extend this analysis to the case of M microphones, where M can be any number greater than 1, and list our findings in Table 2. Appendix B provides the details on how the covariances in Table 2 are computed. Note that when overlapping blocks are used to compute the CSMs, the number of blocks, B, should be replaced by the effective number of blocks, $\omega_1 B$, in Table 2, where ω_1 is used to account for the correlation between overlapping blocks. For instance, for a Hanning window with 50 percent or 75 percent overlap, $\omega_1 = 0.947$ or 0.520, respectively [19]. The covariance matrices

Table 1
Error sources for the DAS beamformer.

Name	Error source	No. of variables
$\mathbf{V}_{\mathrm{CSM}}$ (variables in $\mathbf{G}$)	Random averaging error	M^2
$\mathbf{V}_{\mathrm{Calib}}$ (variables in $\mathbf{C}$)	Calibration errors	$2M$
$\mathbf{V}_{\mathrm{Locs}}$ (microphone locations)	Distance measurement errors	$3M$
V_{Temp} (temperature)	Temperature measurement errors	1

Table 2
Covariances of the CSM variables (the elements in $\mathbf{g}_{\mathrm{CSM}}$).

Variables	Covariance
G_{mm}, G_{mm}	$\lvert G_{mm}\rvert^2/B$
G_{mm}, G_{nn}	$\lvert G_{mn}\rvert^2/B$
G_{mm}, C_{np}	$(C_{mn}C_{mp}+Q_{mn}Q_{mp})/B$
G_{mm}, Q_{np}	$(C_{mn}Q_{mp}-Q_{mn}C_{mp})/B$
C_{mn}, C_{pq}	$(C_{mp}C_{nq}+Q_{mp}Q_{nq}+C_{mq}C_{np}+Q_{mq}Q_{np})/(2B)$
C_{mn}, Q_{pq}	$(C_{mp}Q_{nq}+Q_{mq}C_{np}-Q_{mp}C_{nq}-C_{mq}Q_{np})/(2B)$
Q_{mn}, Q_{pq}	$(C_{mp}C_{nq}+Q_{mp}Q_{mq}-C_{mq}C_{np}-Q_{mq}Q_{np})/(2B)$

due to calibration and location errors are taken as diagonal matrices with the corresponding uncertainties along the diagonals.

When perturbing $\mathbf{G}$ in the Monte-Carlo uncertainty analysis, a Gaussian random vector, say $\tilde{\mathbf{V}}_{\mathrm{CSM}}$, with covariance matrix $\mathbf{g}_{\mathrm{CSM}}$ as given in Table 2 and a zero mean vector is generated every trial (Appendix C briefly discusses one way of doing this) to obtain the perturbations of each variable contained in $\mathbf{V}_{\mathrm{CSM}}$. The perturbation values are then used to form a perturbation matrix $\mathbf{G}_p$ (by properly indexing the variables) and the perturbed CSM is computed as $\mathbf{G}+\mathbf{G}_p$. When perturbing the input variables contained in $\mathbf{V}_{\mathrm{Calib}}$, $\mathbf{V}_{\mathrm{Locs}}$ and V_{Temp}, independent and identically distributed (i.i.d.) Gaussian random variables with zero mean and given uncertainty values are generated, and these perturbations are added to the nominal values.

5. Numerical and experimental results

This section presents the uncertainty analysis of the calibration procedure and the DAS beamformer using numerical as well as experimental data. Both the individual and the cumulative effects of the input parameters are analyzed to understand the dominant sources of uncertainty.

5.1. Microphone array

The microphone array used in our experiments is the large aperture microphone directional array (LAMDA), which is a zero redundancy spiral aperture array built on a 1.82 m diameter rigid aluminum plate, that consists of 90 flush-mounted Panasonic WM-61A electret microphones. LAMDA was designed by the procedures described by Underbrink [20,21] and was fabricated for use in the UFAFF [13]. As shown in Fig. 1, LAMDA contains two nested spiral arrays: (i) a small aperture inner array consisting of 45 microphones and (ii) a larger aperture outer array consisting of 63 microphones. We consider only the outer array in this paper due to its higher resolution at lower frequencies of operation (and refer to it simply as LAMDA). Fig. 2 shows the psf of LAMDA at 2 kHz alongside with the 3-dB beamwidth of the array versus frequency at a broadside distance of $z = 1.48$ m.

5.2. Calibration uncertainty

The uncertainty analysis of the calibration procedure is conducted using Monte-Carlo simulations (a Taylor series based analysis is omitted due to the complexity of the eigen-decomposition and due to the increased flexibility provided by the Monte-Carlo method). The input variables that are perturbed include the CSM, the sound pressure level of the reference microphone, and the individual microphone sensitivities (real-valued and in mV/Pa). The individual microphone

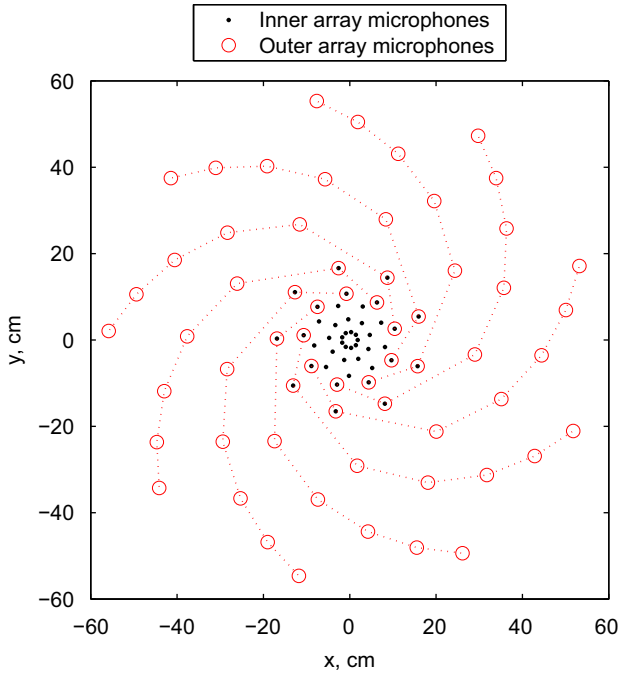

Fig. 1. The microphone layout of LAMDA. The inner and outer arrays consist of 45 and 63 microphones, respectively, sharing 18 microphones.

sensitivities and phases are usually obtained from manufacturer specifications or from individual calibrations with respect to some high quality microphone. We assume that a frequency independent sensitivity value is used for all the microphones with a nominal value of 30 mV/Pa (which is the sensitivity used with the Panasonic WM-61A microphones at the UFAFF), and we assume that the nominal phase of each microphone is 0°. The signal-to-noise ratio (SNR) is set to 25 dB in the calibration setup, where SNR is defined as $10\log_{10}(\sum_{b=1}^{B}\|\mathbf{a}_{\mathrm{cal}}s_{\mathrm{cal}}(b)\|^2)-10\log_{10}(\sum_{b=1}^{B}\|\mathbf{e}(b)\|^2)$. In order to model the uncertainties in the calibration procedure, we simulate microphone pressure measurements from an ideal monopole source located at (0, 0, 1.48) m. The array center is located at (0, 0, 0) m (nominally). The sampling frequency f_s = 65,536 Hz and the block length H=4096. All B values shown represent effective number of blocks. The frequency is set at 5 kHz, and 1000 Monte-Carlo trials have been implemented. Due to the observation that the output distributions are Gaussian, 2 times the sample standard deviation is considered as the uncertainty in the plots of this section.

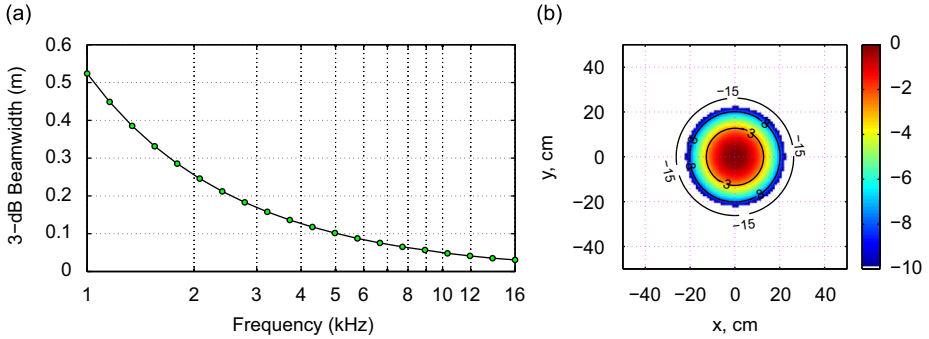

Fig. 2. (a) The 3-dB beamwidth of LAMDA versus frequency and (b) the psf at 2 kHz. The levels are in normalized dB in (b) the array broadband distance is z = 1.48 m.

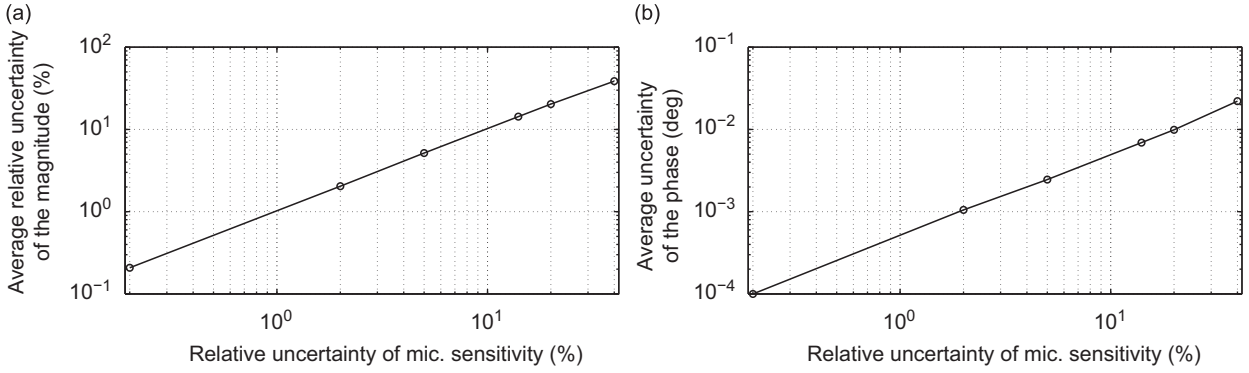

Fig. 3. The average (over all microphones) uncertainty of the magnitude and phase terms of the microphone correction factors when the individual microphone sensitivities are perturbed. Frequency is 5 kHz.

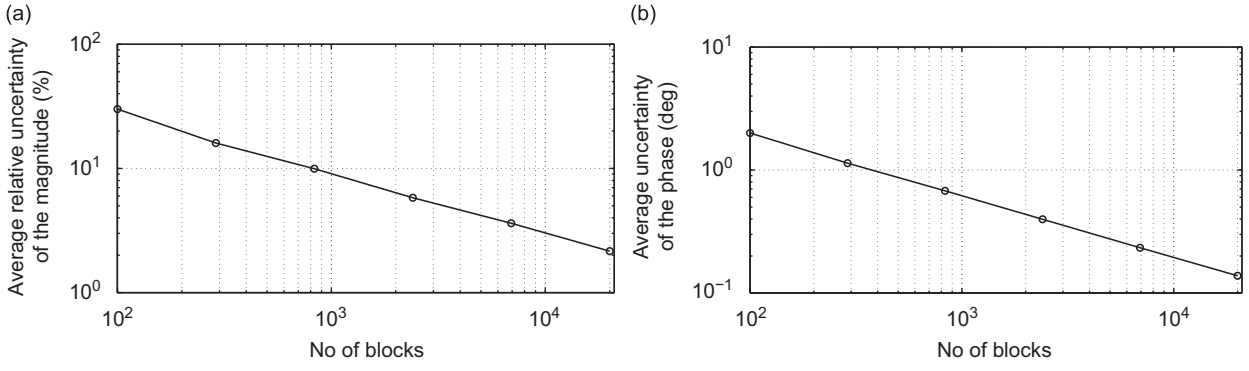

Fig. 4. The average (over all microphones) uncertainty of the magnitude and phase terms of the microphone correction factors when the CSM is perturbed. Frequency is 5 kHz.

First, we consider the effects of perturbing the individual microphone sensitivities while keeping the other input variables at their nominal values. As observed from Fig. 3, there is a one-to-one relationship between the relative uncertainties in the microphone sensitivities and the magnitude of the calibration factors. In the figures presented in this

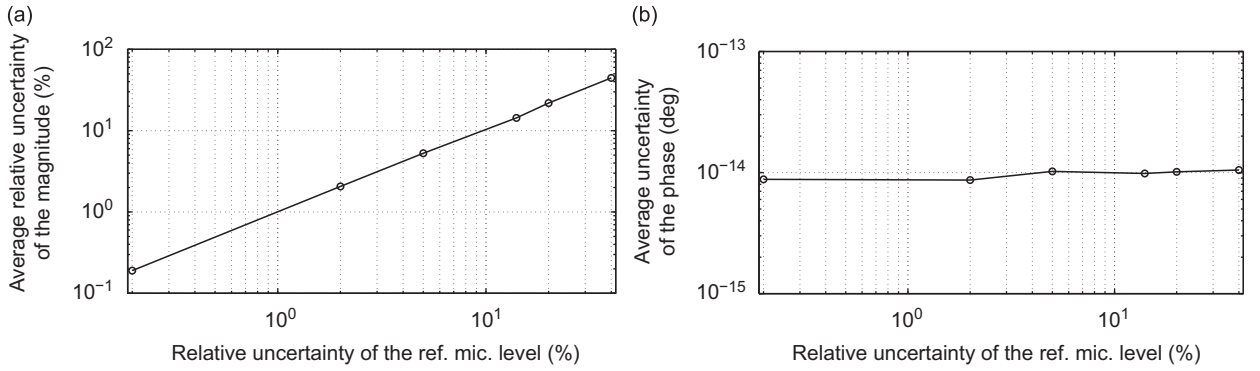

Fig. 5. The average (over all microphones) uncertainty of the magnitude and phase terms of the microphone correction factors when the reference microphone level is perturbed. Frequency is 5 kHz.

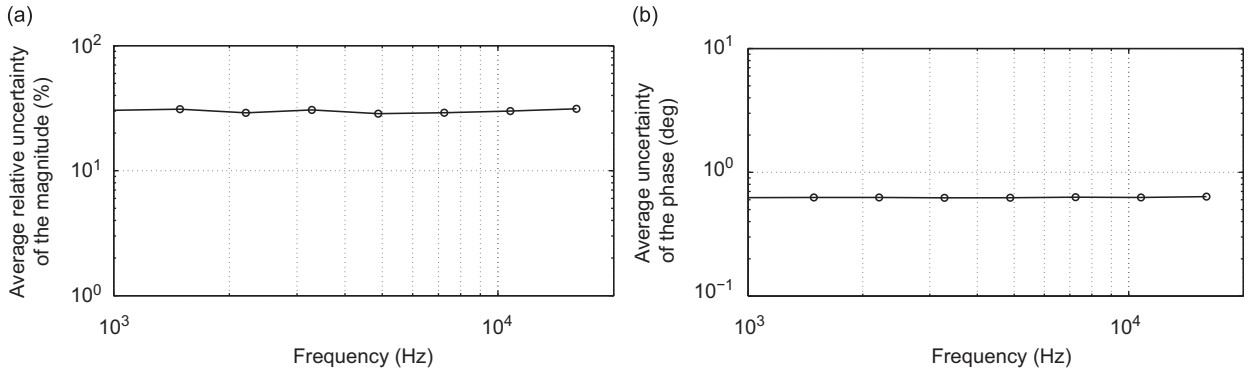

Fig. 6. The average (over all microphones) uncertainty of the magnitude and phase terms of the microphone correction factors for varying frequency where the relative uncertainty in microphone sensitivities and reference microphone level are 10 percent and the number of blocks is 1000.

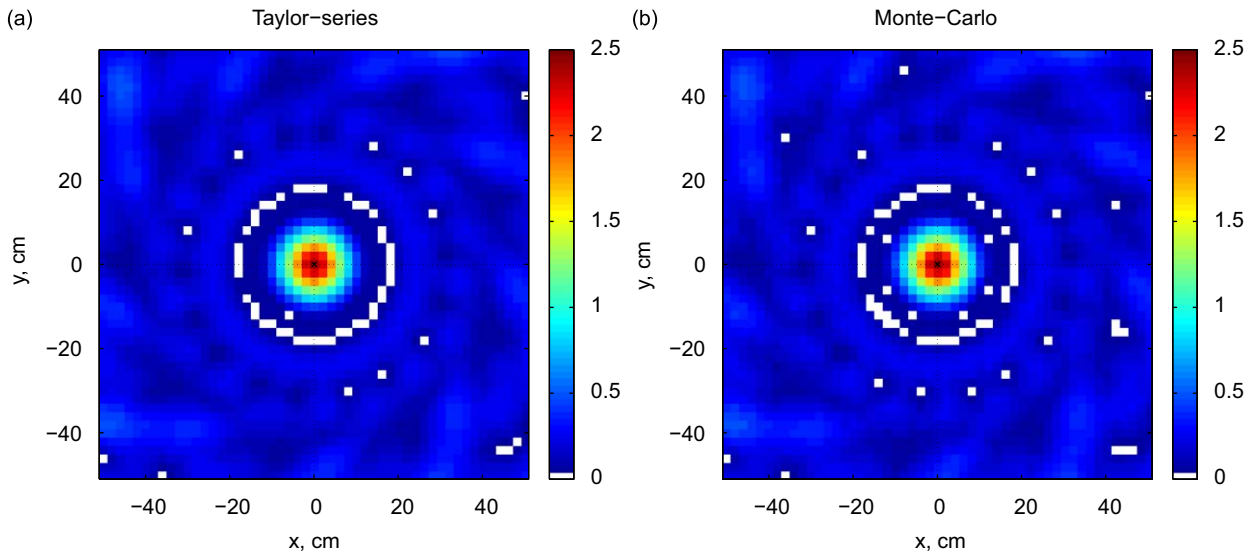

Fig. 7. The difference in dB between the true source power, P_0, and $P_0+2\sigma_l$, where σ_l is the sample standard deviation estimated via each of the two methods at the l th scanning point. The relative uncertainty of the microphone correction factor magnitude is 5 percent and the uncertainty of the microphone correction factor phase is 1°. Frequency is 5 kHz.

section, the average (over all microphones) uncertainty in the magnitude and phase of the microphone correction factors are plotted. Note that the averages are taken after finding the uncertainty of each individual microphone. One important note here is that a higher uncertainty is not necessarily detrimental since the goal of calibration is to correct for such errors. Therefore, we find it more appropriate to consider the effects of microphone sensitivity and phase errors, temperature errors and microphone location errors in the following sections of the paper where we analyze the overall DAS uncertainty.

The effect of the number of blocks, B, on the uncertainty of the calibration procedure can be observed from Fig. 4, where all the other variables are kept at their nominal values. There is approximately a one-to-two ratio in the uncertainties as expected since the error in the CSM drops with $\sqrt{B}$. Although the uncertainties in the magnitude appears to be large (10 percent) for a conventional B such as 1000, the final effect on the DAS estimate is within reasonable limits as will be shown below. For instance, with a nominal sensitivity of 30 mV/Pa, a positive 10 percent perturbation in all the microphone sensitivities will yield $|20\log_{10}(30/33)| = 0.83$ dB difference in the source levels. We observe that the phase uncertainty is relatively low even for small B.

Next, we examine the uncertainties in the reference microphone sound pressure levels only in Fig. 5. Such errors might rise from the imperfect calibrations of the reference microphone. As expected, there is a one-to-one relation between the calibration uncertainty and the reference microphone level uncertainty. The phase is not affected since the second stage of calibration is for magnitude correction only.

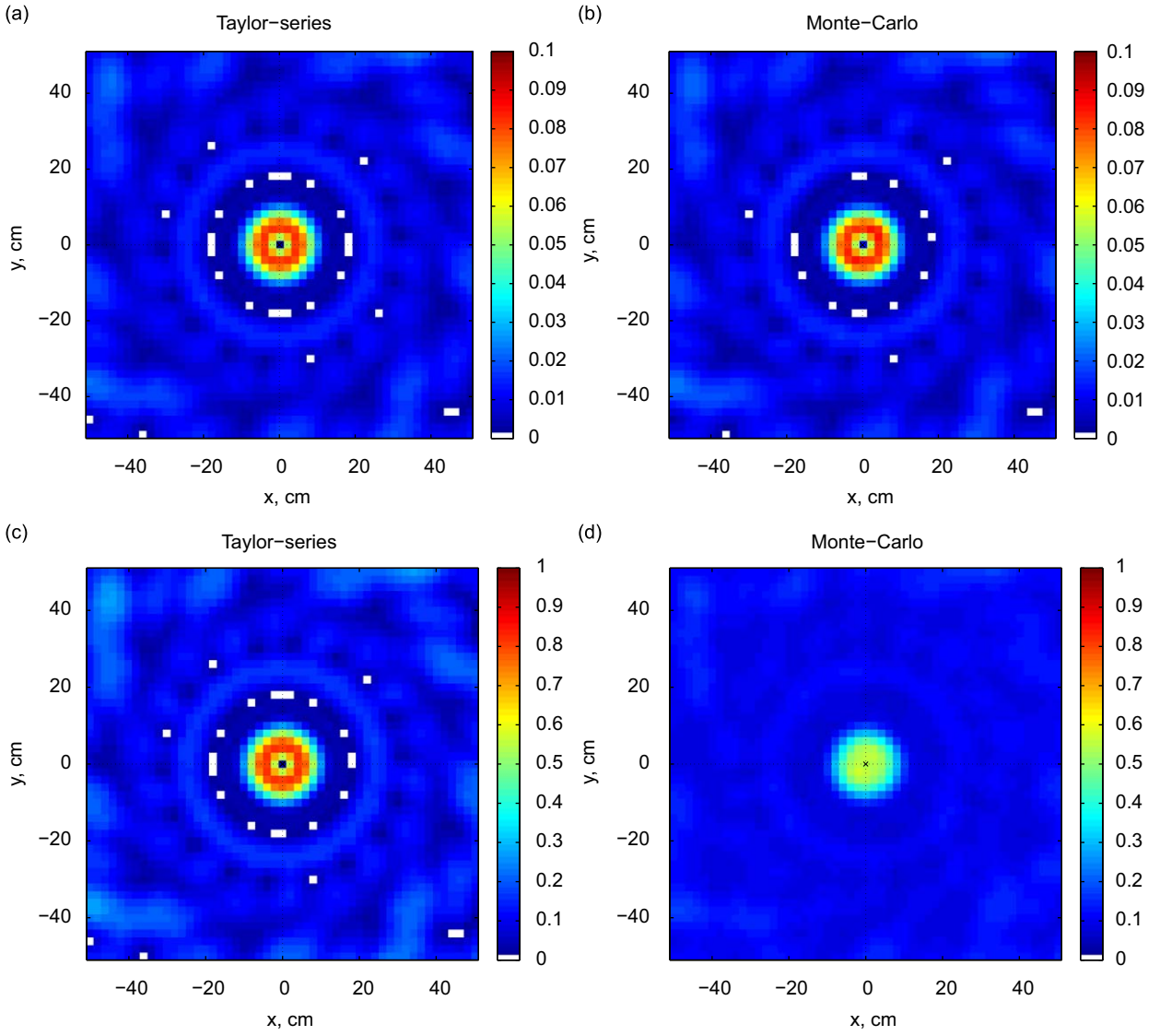

Fig. 8. The difference in dB between the true source power, P_0, and $P_0+2\sigma_l$, where σ_l is the sample standard deviation estimated via each of the two methods at the l th scanning point. The microphone locations are perturbed with i.i.d. Gaussian random variables of standard deviations 1 mm in (a) and (b), and 10 mm in (c) and (d). Frequency is 5 kHz.

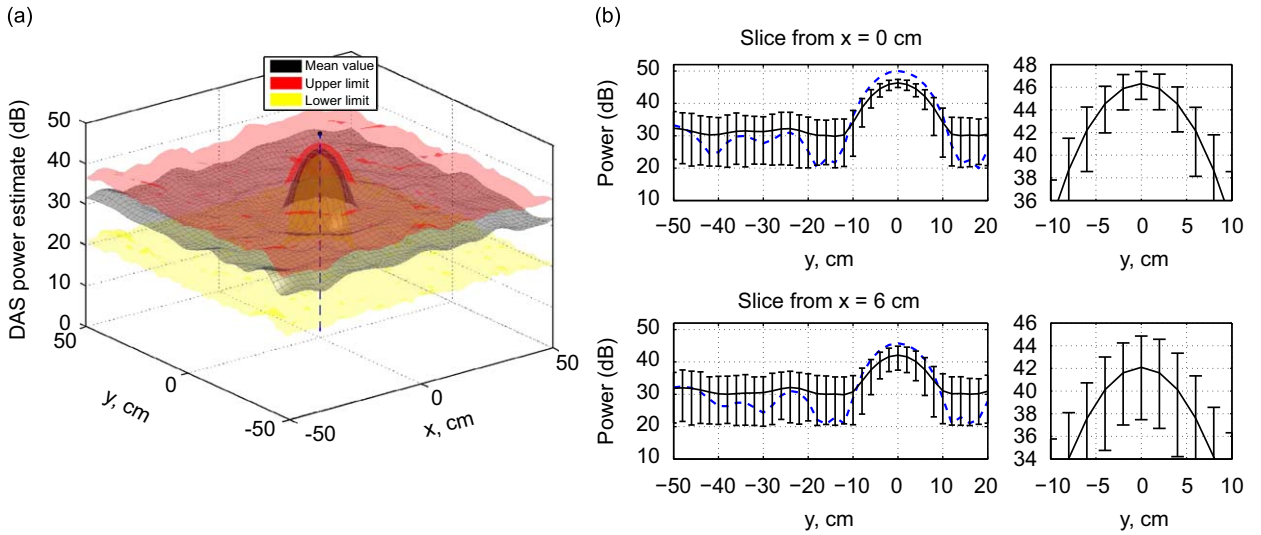

Fig. 9. Microphone locations are perturbed with a standard deviation of 10 mm. (a) 3D plot showing the mean and the 95 percent confidence intervals. The true source location and power are indicated with the dashed line and the dot at its tip, respectively. (b) Two slices from the plot in (a) to further illustrate the 95 percent confidence intervals. The black solid line and the blue dashed line indicate the mean values and the nominal values, respectively. A zoomed in view of the main beam region is also provided. Frequency is 5 kHz. (For interpretation of the references to color in this figure legend, the reader is referred to the web version of this article.)

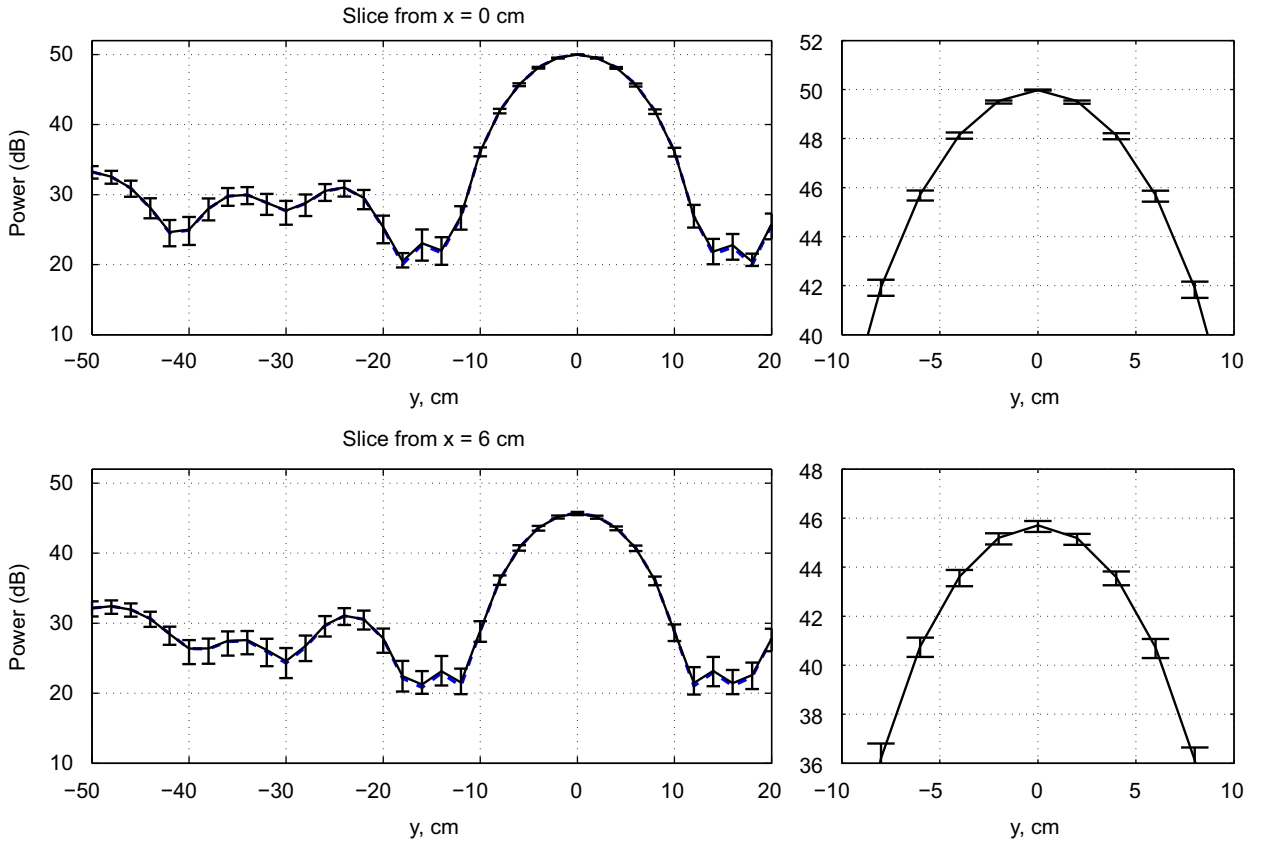

Fig. 10. Profile plots of the mean and the 95 percent confidence intervals when microphone locations are perturbed with a standard deviation of 1 mm. The black solid line and the blue dashed line indicate the mean values and the nominal values, respectively. A zoomed in view of the main beam region is also provided. The nominal and the mean values are indistinguishable at most *y* values. Frequency is 5 kHz. (For interpretation of the references to color in this figure legend, the reader is referred to the web version of this article.)

Finally, in Fig. 6, where the uncertainties in the microphone sensitivities and reference microphone level are set to 10 percent and $B=1000$, the uncertainty of calibration with varying frequency is plotted. It is observed that the uncertainty is independent of frequency. This is because the microphone sensitivity and reference microphone level uncertainties are assumed to be frequency-independent in our analysis. (Note that in practice, the uncertainties might vary somewhat with frequency, in which case the calibration uncertainty will also vary with frequency.) In the next section, we will see that when the microphone locations or the temperature are perturbed, the frequency will be important since these perturbations will be multiplied by the wavenumber.

Based on the above observations, the accurate calibration of the reference microphone is very important since this will determine the array power estimates directly. Moreover, it appears that during calibration, it is beneficial to acquire data for as long as possible. As mentioned above, the uncertainties in calibration due to microphone sensitivity and phase errors, temperature errors and microphone location errors are better analyzed within the context of beamforming.

5.3. DAS uncertainty

Unless otherwise stated, in all the simulations in this section, a monopole source with 50 dB signal power (power is defined at the nominal array center) is simulated at (0, 0, 1.48) m where the array center is nominally located at (0, 0, 0) m as in the calibration case. (Note that the calibration speaker at UFAFF produces approximately 50 dB signal power at the array center.) One thousand Monte-Carlo trials have been implemented (see Appendix D for an analysis on the number of

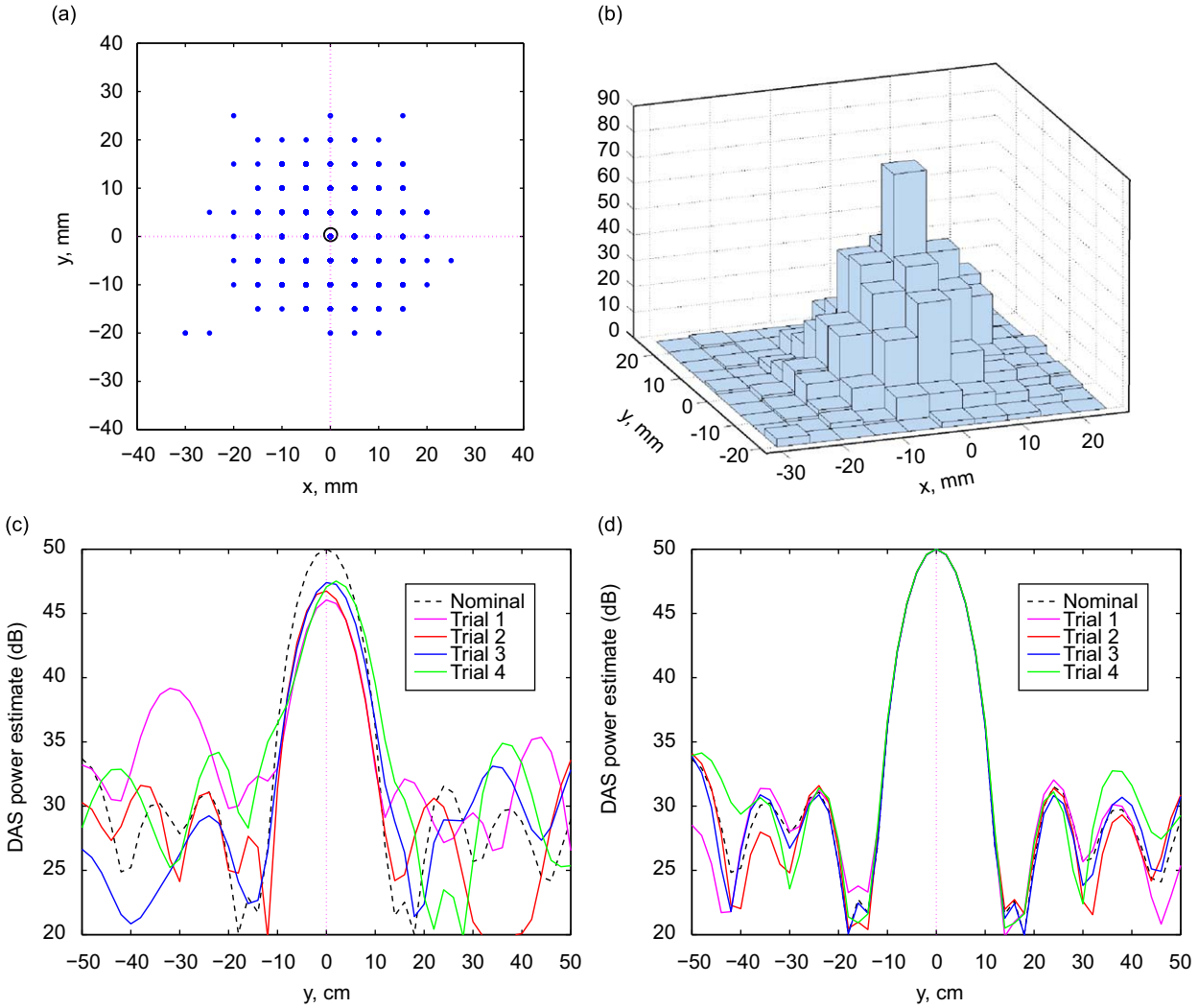

Fig. 11. Microphone locations are perturbed with a standard deviation of 10 mm. (a) The location of the DAS peak estimate at each Monte-Carlo trial is marked with a dot and the mean location of the peaks is marked with the empty circle. (b) The histogram of the locations of the peaks. (c) and (d) The DAS power estimates at four arbitrary trials together with the nominal estimate. No calibration is applied in (a)–(c) and calibration is applied in (d). Slices from the beamforming images at $x = 0$ m are shown in (c) and (d). Note that the units in (a) and (b) are in mm. Frequency is 5 kHz.

Monte-Carlo iterations used) and the frequency is set at 5 kHz. The SNR is 25 dB. The scanning region is set from -0.50 to 0.50 m with 0.02 m resolution in both the x and y directions. The room temperature is T_0 = 293 K and the nominal sound speed is 343 m/s.

5.3.1. Comparison of the multivariate and Monte-Carlo methods

In this section we show that the multivariate and Monte-Carlo uncertainty analysis of the DAS beamformer yield consistent results when the perturbations are relatively low and that the two methods differ when the perturbations become larger. We consider the perturbations in the calibration factors and the microphone locations, and similar conclusions can be made when the CSM and microphone correction factors are perturbed.

In order to analyze the effects of the calibration uncertainty on the DAS estimates, we perturb $\tilde{\mathbf{D}}$ (see Eq. (8)) using the values obtained in Section 5.2 as a guideline. The uncertainties in the real and imaginary components of the calibration factors can be found by either using a simple Monte-Carlo analysis or using multivariate uncertainty propagation given the uncertainties in magnitude and phase [18]. The resulting sample covariance matrix from this procedure is then used to generate (possibly correlated) perturbation values for D_m and E_m at each Monte-Carlo iteration, where $m = 1, \ldots, M$. Fig. 7 shows the difference in dB between the true source power, P_0, and $P_0 + 2\sigma_l$, where σ_l is the sample standard deviation estimated via each of the two methods at the l th scanning point. The results of the two methods match well and it was observed that this is the case even for large perturbation values in microphone calibration factors (results not shown).

Next, we consider two perturbation settings for the microphone locations. The microphone locations are perturbed with i.i.d. Gaussian random variables of standard deviations 1 and 10 mm in Figs. 8(a)–(b) and (c)–(d), respectively. It is observed that the two uncertainty analysis methods give different results when the perturbations are larger. Note that 1 and 10 mm perturbations translate into relative uncertainties of 0.2 percent and 2.3 percent, respectively, in terms of microphone to source distances.

As the uncertainties in the input variables increase, the first-order linear approximation with the Taylor series does not suffice to model the overall uncertainty due to the nonlinearities. To increase the accuracy of this method, more terms need to be considered in the Taylor series expansion [11]. However, the algebra can quickly become cumbersome for Eq. (8). Even if the Taylor series expansion involved as many terms as needed, when the resulting distributions are not Gaussian,

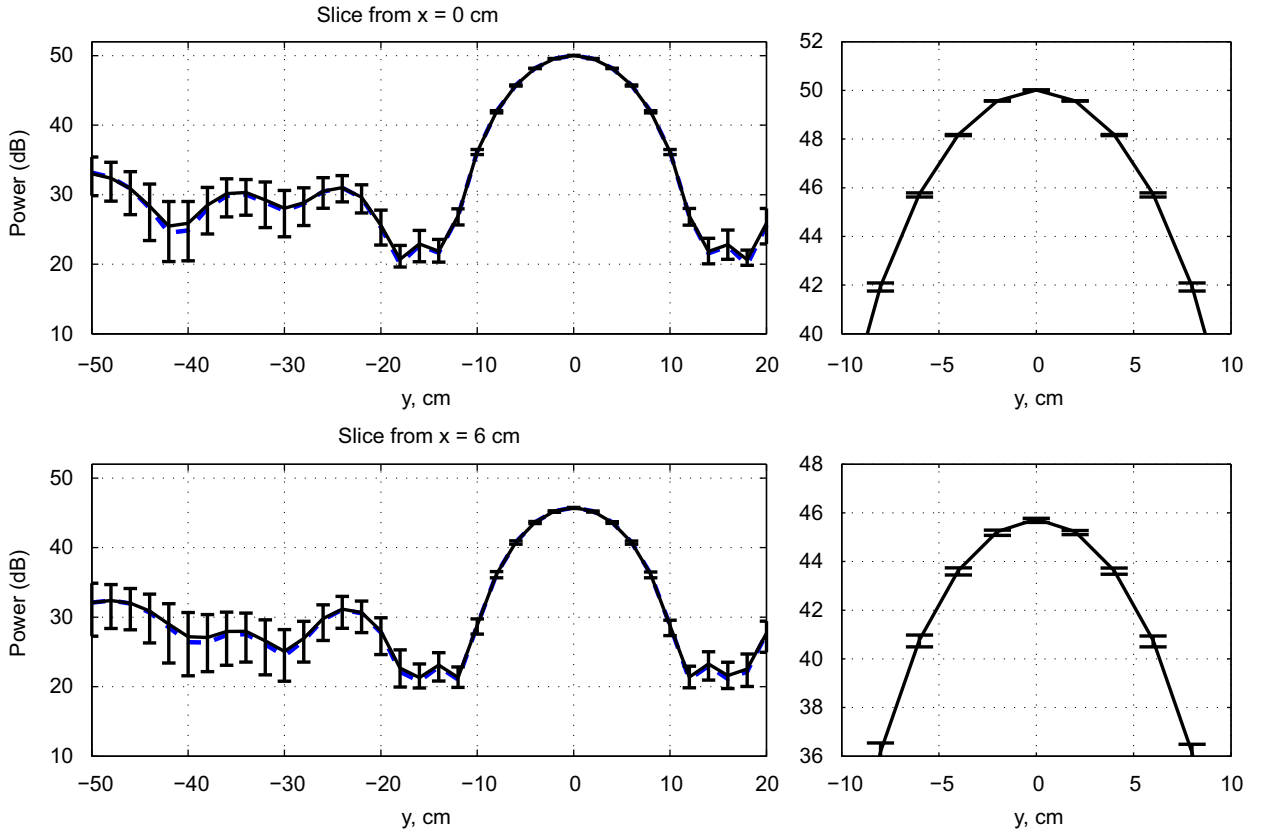

Fig. 12. Profile plots of the mean and the 95 percent confidence intervals when microphone locations are perturbed with a standard deviation of 10 mm and calibration is applied. The black solid line and the blue dashed line indicate the mean values and the nominal values, respectively. A zoomed in view of the main beam region is also provided. The nominal and the mean values are indistinguishable at most y values. Frequency is 5 kHz. (For interpretation of the references to color in this figure legend, the reader is referred to the web version of this article.)

the standard deviation estimates of the multivariate method cannot be used to obtain 95 percent confidence intervals. These limitations and some other reasonings provided below make Monte-Carlo analysis a better candidate for analyzing the DAS beamformer uncertainty.

5.3.2. Monte-Carlo based uncertainty analysis

This section considers the uncertainty of the DAS beamformer using Monte-Carlo simulations. We consider the uncertainties in microphone sensitivity and phase, microphone location, array broadband distance, temperature and CSM. In the multivariate uncertainty method, the calibration effects had to be analyzed through $\tilde{\mathbf{D}}$. However, in the Monte-Carlo method, $\tilde{\mathbf{D}}$ will be estimated from calibration, which is done at each Monte-Carlo iteration using the perturbed inputs, and directly substituted in the data reduction equation. In the Monte-Carlo method, we estimate the distribution of the DAS power estimates at each scanning point and then obtain the 95 percent confidence intervals and mean values. Then, these values are converted into dB. The reason for showing 95 percent confidence intervals instead of sample standard deviations is that the resulting distributions are in general asymmetrical about their mean values. For instance, for a scanning point where the DAS estimate is relatively low, since the power estimate is constrained to be positive, ± 2 times the standard deviation cannot be used to obtain the confidence intervals when the mean is less than twice the standard deviation. The 95 percent confidence intervals are therefore best estimated from the distributions and standard deviations might be insufficient in modeling the uncertainties.

First, we investigate the microphone location uncertainty in detail while keeping the other input variables at their nominal values. Figs. 9 and 10 show the 95 percent confidence intervals at each scanning point when the x, y and z components of the microphone locations are perturbed using i.i.d. Gaussian random variables with zero means and standard deviations of $\sigma_{\text{Locs}} = 10$ mm and $\sigma_{\text{Locs}} = 1$ mm, respectively. These perturbation values can be normalized by the wavelength (at 5 kHz) to obtain dimensionless values of 0.146 (for 10 mm) and 0.015 (for 1 mm). Note that calibration is not applied in these plots. The 3D plot in Fig. 9(a) shows the mean, and the upper and lower limits of the 95 percent confidence intervals at each scanning location. The true source location and power are indicated with the dashed line and the dot at its tip, respectively. The 2D plot in Fig. 9(b), on the other hand, shows two slices from the 3D plot taken at $x = 0$ and 0.06 m. (The 3D plot is omitted in the rest of the examples since the 2D profiles appear to be more informative.)

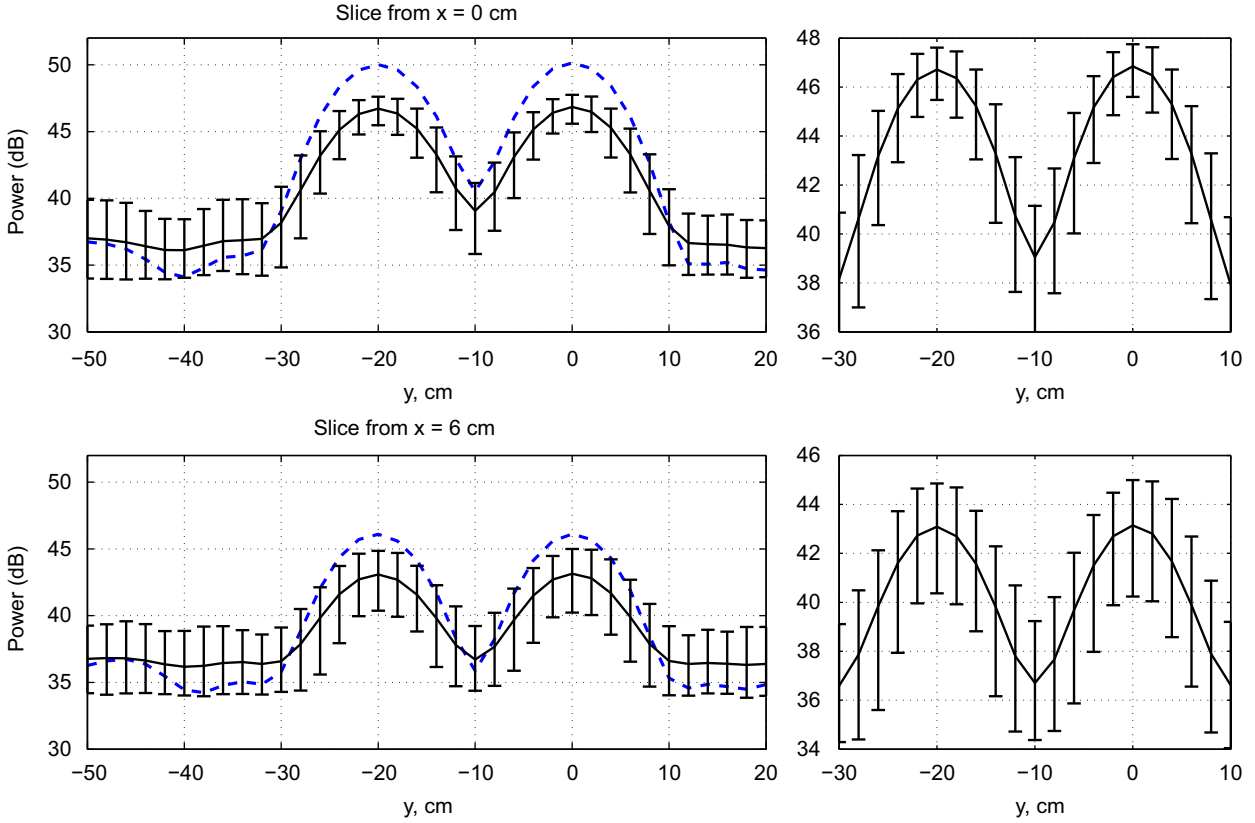

Fig. 13. Two sources are placed at (0, 0, 1.48) m and (0, −0.20, 1.48) m with equal strengths of 50 dB. Profile plots of the mean and the 95 percent confidence intervals when microphone locations are perturbed with a standard deviation of 10 mm and calibration is not applied. The black solid line and the blue dashed line indicate the mean values and the nominal values, respectively. A zoomed in view of the main beam region is also provided. Frequency is 5 kHz. (For interpretation of the references to color in this figure legend, the reader is referred to the web version of this article.)

Note that in the 2D plots, the confidence intervals in the region from $y=0.2$ to 0.5 m are omitted since they resemble closely the confidence intervals in the region from $y=-0.5$ to 0.2 m. Instead, a zoomed in view of the main beam, which is of relatively more interest, is provided (the nominal curve is omitted in the zoomed in plots). One important observation that can be made from Fig. 9 is that the power estimates are biased downwards with respect to the nominal value. Appendix E provides an explanation for this rather non-intuitive phenomenon. To further elaborate on the bias issue, we show the peak location of the DAS beamforming image at each Monte-Carlo trial when $\sigma_{\text{Locs}}=10$ mm together with the histogram of the peak location in Figs. 11(a) and (b). Note that the DAS peak location exhibits a discrete pattern due to the finite scanning resolution which is set to 5 mm in Fig. 11(a). The mean of the peak locations over all the trials is indicated with the empty circle. It is observed that the DAS peak occurs either at the true source location or in its vicinity and that the mean location of the peaks coincides with the true source location. However, even when the peak appears at the true source location, the estimated power value is less than the nominal value (as discussed in Appendix E). This can also be observed from Fig. 11(c) where slices from the beamforming map at $x=0$ m from four different samples are shown together with the nominal value. We observe that there are large fluctuations at almost every scanning point due to the location errors, consistent with the plots in Fig. 9.

As observed above, microphone location errors can cause significant problems if not accounted for. Since calibration is specifically designed for such errors, we expect it to improve the results. In Fig. 12, we again show the 95 percent confidence intervals at each scanning point but now with calibration applied. It is observed that calibration greatly reduces the variations of the DAS power estimates due to location errors. Fig. 11(d) shows that the power estimates from trial-to-trial now line up nicely as opposed to Fig. 11(c). When finding the calibration factors, we assumed that all the input variables except the microphone locations are at their nominal values.

To analyze the performance of the calibration in the presence of sources at different locations than the calibration speaker, we consider a scenario where two monopole sources of equal strength (50 dB) are placed at (0, 0, 1.48) m and (0, −0.20, 1.48) m. In Figs. 13 and 14, the 95 percent confidence intervals are shown when calibration is not applied and when calibration is applied, respectively. Similar observations to the single source case can be made. It seems that although the second source is not at the same location as the calibration speaker, calibration still helps to reduce the uncertainties.

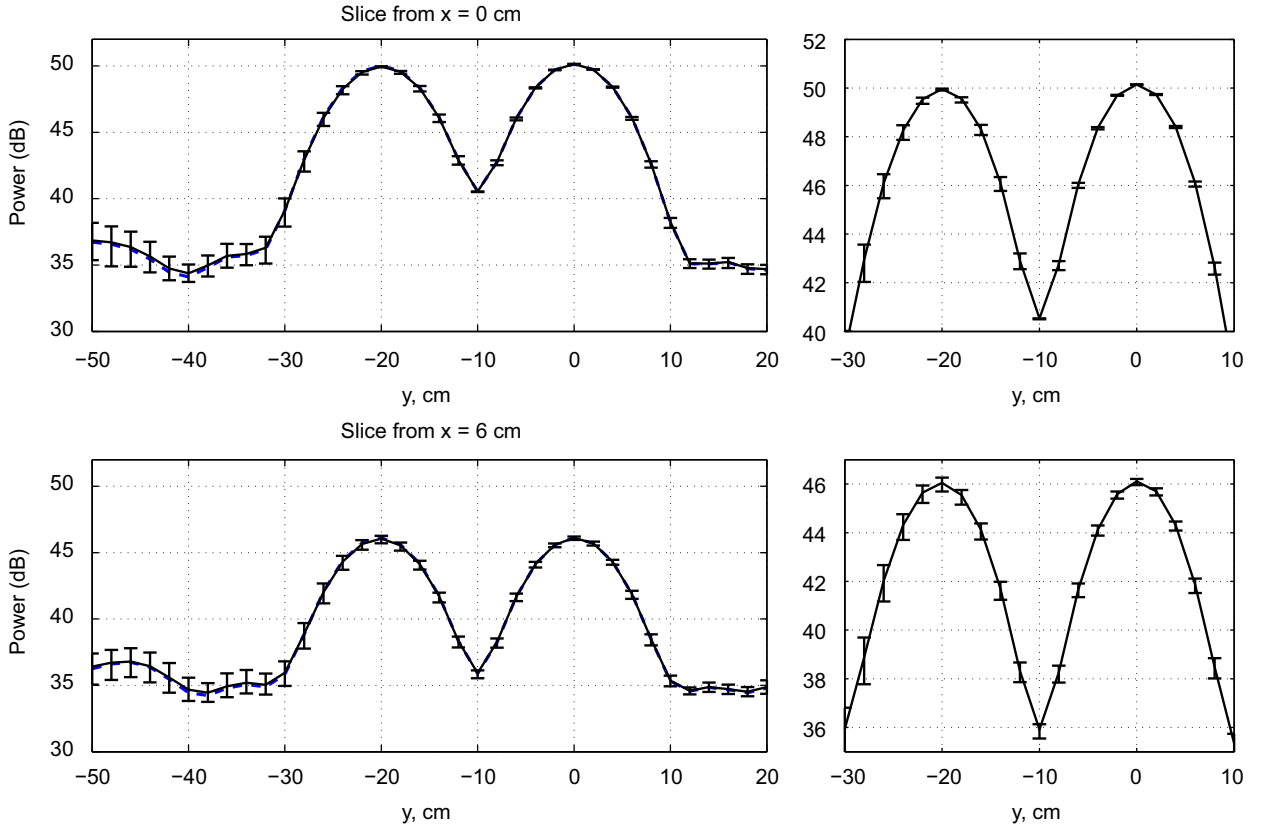

Fig. 14. Two sources are placed at (0, 0, 1.48) m and (0, −0.20, 1.48) m with equal strengths of 50 dB. Profile plots of the mean and the 95 percent confidence intervals when microphone locations are perturbed with a standard deviation of 10 mm and calibration is applied. The black solid line and the blue dashed line indicate the mean values and the nominal values, respectively. A zoomed in view of the main beam region is also provided. The nominal and the mean values are indistinguishable at most y values. Frequency is 5 kHz. (For interpretation of the references to color in this figure legend, the reader is referred to the web version of this article.)

The application of calibration thus seems essential when we anticipate errors in our location measurements. Even though the location errors of the microphones on the array plane, i.e., in the x and y directions, can be measured very accurately, the non-uniformity of the array surface can result in unknown location errors. In the examples considered above, we assumed that the temperature was the same in the calibration and test data. However, in the presence of flow, the non-uniformity of temperature in the test section will cause sound speed differences in the calibration and test cases.

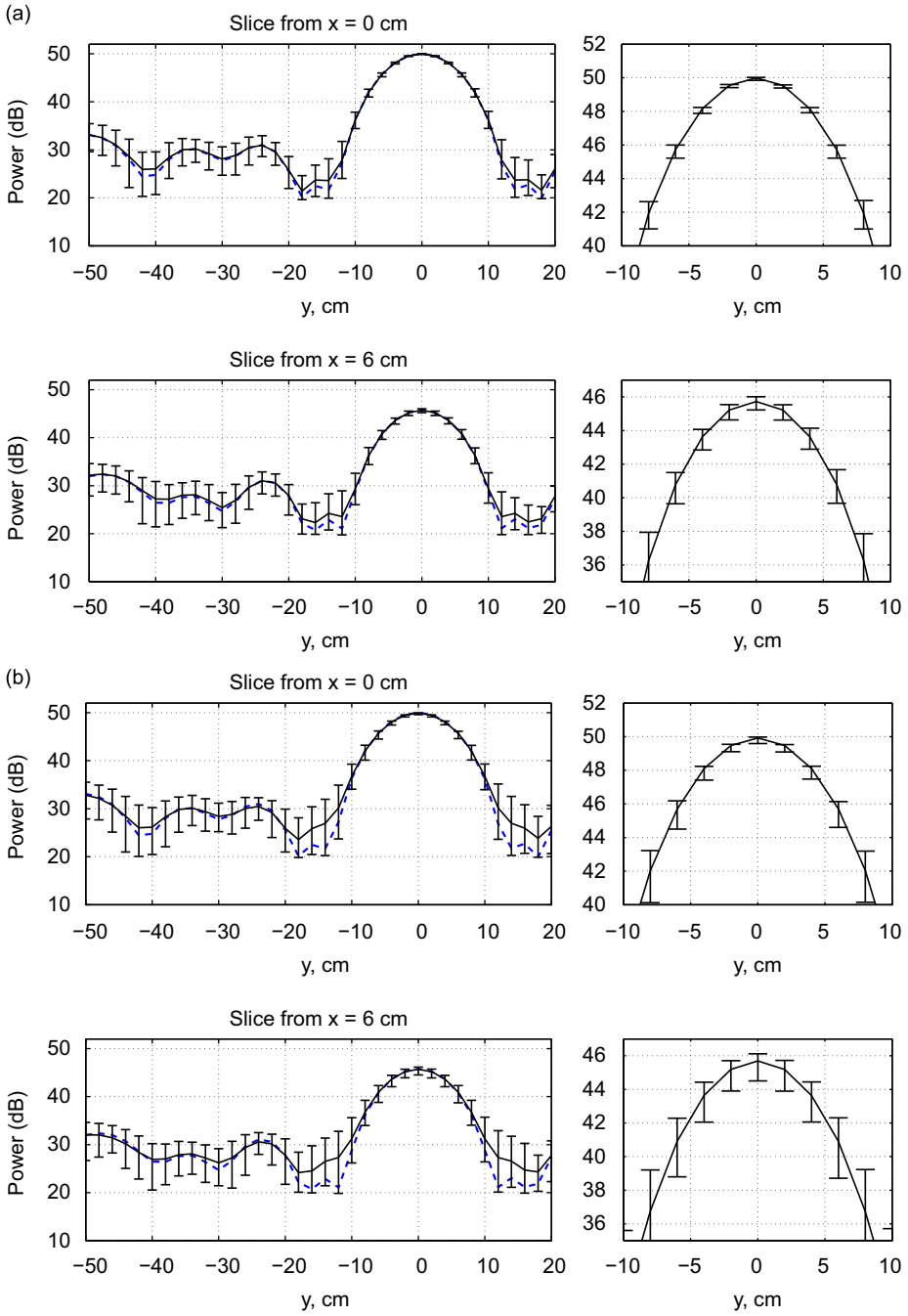

Fig. 15. The 95 percent confidence intervals of the DAS power estimates when the array broadband distance is perturbed. Two slices from the beamforming image at $x = 0$ and 6 cm are considered. The relative uncertainty in array broadband distance is (a) 2.5 percent, and (b) 5 percent. The black solid line and the blue dashed line indicate the mean values and the nominal values, respectively. A zoomed in view of the main beam region is also provided. The nominal and the mean values are indistinguishable at some y values. Frequency is 5 kHz. (For interpretation of the references to color in this figure legend, the reader is referred to the web version of this article.)

Furthermore, in practice, there is a certain uncertainty associated with the array broadband distance, especially with complex test models.

To represent the uncertainty in the model to array distance, we perturb the array broadband distance together with the array microphone locations, and apply calibration as before. Figs. 15(a) and (b) show the 95 percent confidence intervals when the relative uncertainties in the array broadband distance are set to 2.5 percent and 5 percent, respectively. Note that in our case, these correspond to net uncertainties of 0.04 and 0.07 m. Keeping in mind that the nominal broadband distance of the source is 1.48 m, such errors might be realizable in practice, especially when testing models with complex geometries. We also analyze the deterministic error in the estimated power levels when the array broadband distance is varied. Fig. 16 shows the power estimated at $(x, y) = (0, 0)$ m when the array broadband distance is varied from 1.1 to 1.9 m with increments of 0.5 mm. It is observed that the estimated source levels exhibit a concave behavior with a peak at the true source height.

In Fig. 17, we analyze the 95 percent confidence intervals when the number of blocks B used in computing the CSM is varied and the other variables are kept at their nominal values. The calibration CSM is also perturbed assuming that the number of blocks used for the calibration was 1000. We observe that $B=1000$ case reduces the uncertainty by about 0.5 dB compared to the $B=200$ case.

Figs. 18 and 19 show the 95 percent confidence intervals when the individual microphone sensitivities and phases are perturbed. It is assumed that the microphone sensitivities and phase values remain the same during calibration and testing. We observe that the uncertainties are somewhat large for 15 percent relative uncertainty in the microphone sensitivities and that when the calibration input variables are at their nominal values, the phase errors are corrected accurately.

Fig. 20 shows the 95 percent confidence intervals when the temperature is perturbed. In practice, the errors in temperature will be negligible during calibration due to the absence of flow. However, during model testing, the temperature uncertainty could be significant. Here we consider 0.1 °C (Fig. 20(a)) and 3 °C (Fig. 20(b)) uncertainty in temperature during testing and 0.1 °C uncertainty during calibration. It appears that the beamforming procedure is quite insensitive to temperature uncertainties provided that calibration is applied. Note that a 3 °C uncertainty in temperature will cause a relative perturbation of 0.5 percent in sound speed. We emphasize that the temperature uncertainty has only been considered through its effect on the sound speed. In practice, microphone transfer functions as well as microphone locations (due to the expansion/contraction of the array plate) could be affected by temperature, resulting in larger uncertainties.

Finally, in Fig. 21 we consider the overall uncertainty when the microphone location uncertainties are 10 mm, relative array broadband distance uncertainty is 5 percent, temperature uncertainty is 3 °C for testing and 0.1 °C for calibration, CSM uncertainty is calculated using 1000 blocks for both calibration and testing, and microphone sensitivity and phase uncertainties are 15 percent and 10°, respectively. It is observed that the 95 percent confidence interval at the source location is around $[-0.84, 0.45]$ dB of the mean value.

5.3.3. *Monte-Carlo based uncertainty analysis of experimental data*

The Monte-Carlo method is now demonstrated on experimental data taken at the UFAFF using LAMDA with the purpose of investigating the uncertainty in the integrated DAS levels. The integrated power level is computed by summing the DAS power estimates inside the integration region (which is within the scanning region) and normalizing the result by a scaling factor obtained by summing the psf values (see Section 2.2) over the same integration region. Stated mathematically, the

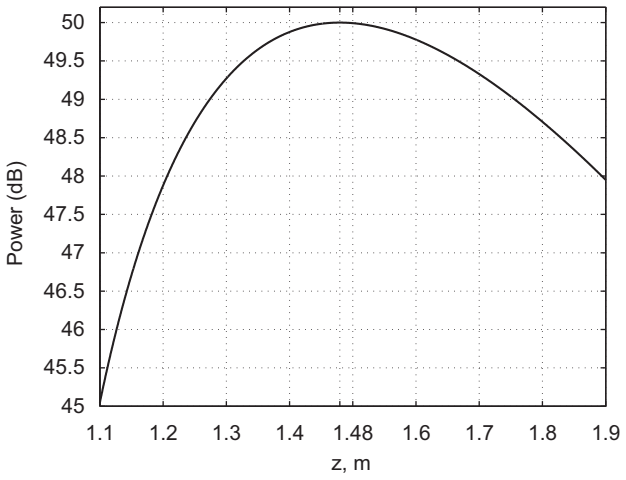

Fig. 16. The power estimated at $(x, y) = (0, 0)$ m when the array broadband distance (in particular, z) is varied from 1.1 to 1.9 m with increments of 0.5 mm. The true source distance to array is 1.48 m and the true source power is 50 dB. Frequency is 5 kHz.

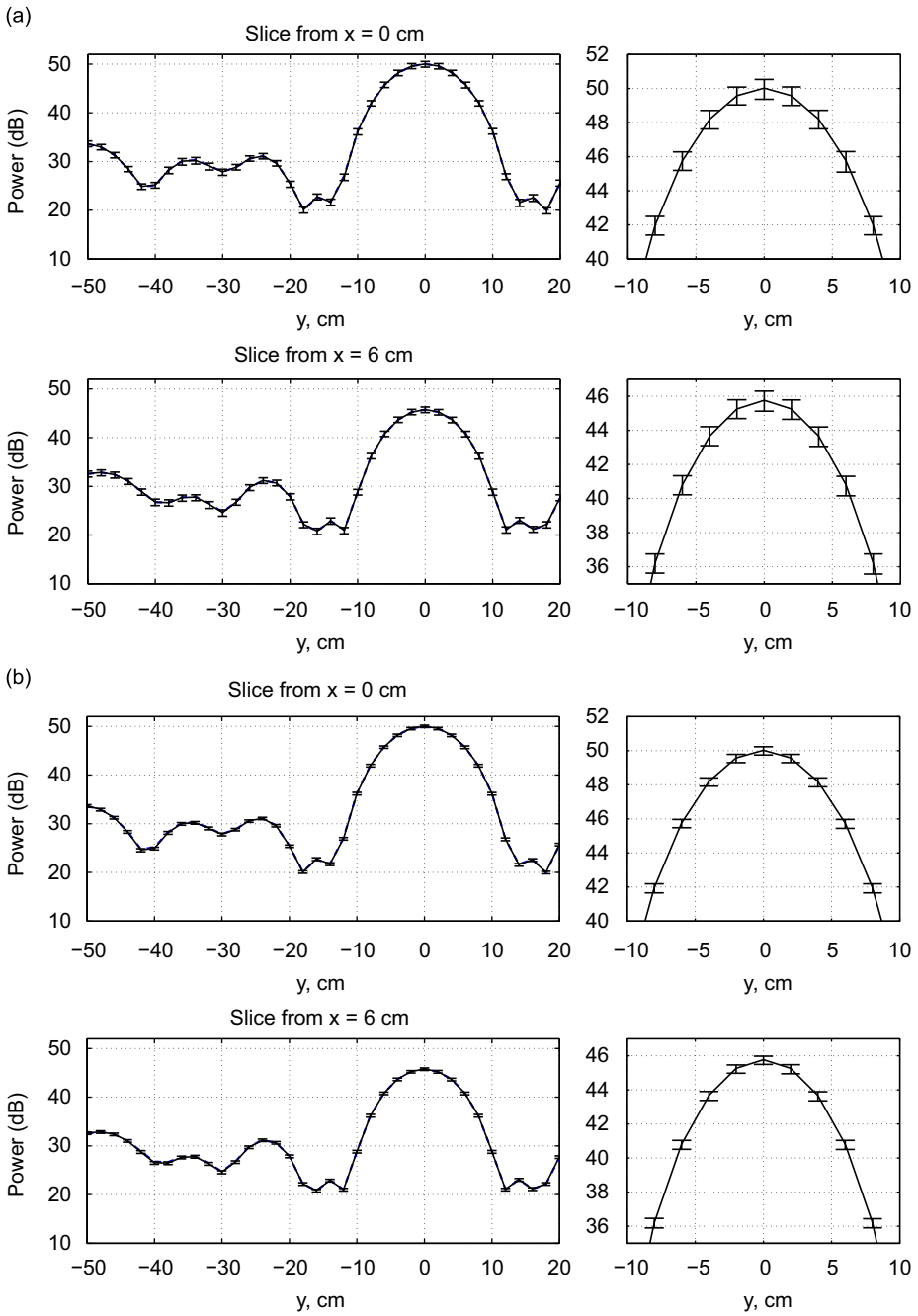

Fig. 17. The 95 percent confidence intervals of the DAS power estimates when the CSM is perturbed. Two slices from the beamforming image at $x = 0$ and 6 cm are considered. Number of blocks are (a) $B=200$ and (b) $B=1000$. The black solid line and the blue dashed line indicate the mean values and the nominal values, respectively. A zoomed in view of the main beam region is also provided. The nominal and the mean values are indistinguishable at most y values. Frequency is 5 kHz.(For interpretation of the references to color in this figure legend, the reader is referred to the web version of this article.)

integrated DAS level is defined as $\sum_{l\in\mathcal{L}} P_l / \sum_{l\in\mathcal{L}} \mathrm{psf}(l)$, where $\mathcal{L}$ is a set containing the indices of the scanning grid points within the integration region [22,23]. In the Monte-Carlo trials, the normalization factor is calculated at each iteration with the perturbed values.

The first test setup consists of a single speaker placed at (0, 0, 1.48) m similar to the scenario considered earlier with simulations. The data analysis parameters are as follows: a Hanning window with 75 percent overlap has been applied to blocks of size 4096 samples, the sampling frequency is 65,536 Hz and the data acquisition time is 15 s resulting in 498 effective blocks and a frequency resolution of 16 Hz. The scanning region extends from -0.50 to 0.50 m with a resolution of

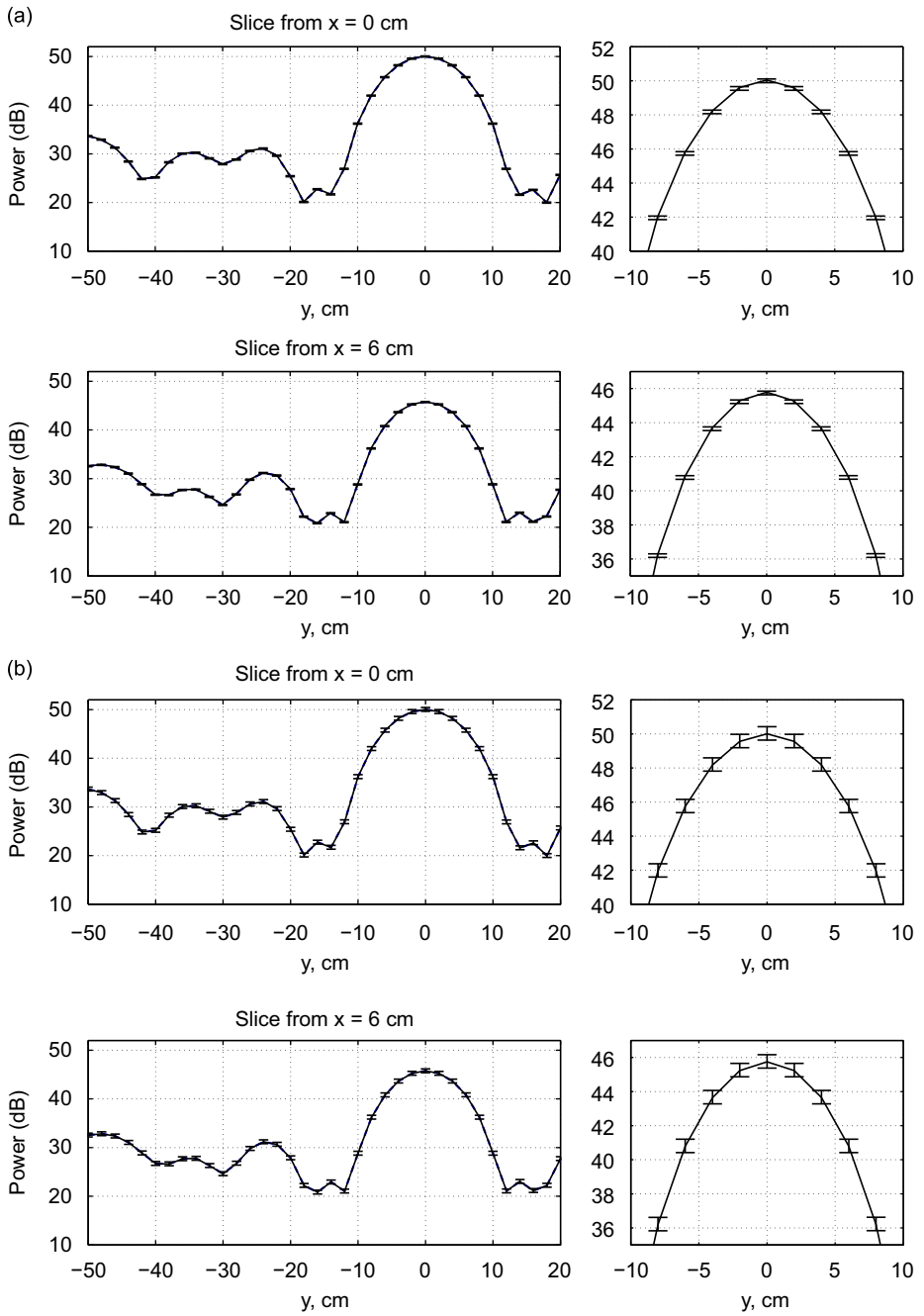

Fig. 18. The 95 percent confidence intervals of the DAS power estimates when the individual microphone sensitivities are perturbed. Two slices from the beamforming image at $x = 0$ and 6 cm are considered. The relative input uncertainties are (a) 5 percent, and (b) 15 percent. The black solid line and the blue dashed line indicate the mean values and the nominal values, respectively. A zoomed in view of the main beam region is also provided. The nominal and the mean values are indistinguishable at most y values. Frequency is 5 kHz. (For interpretation of the references to color in this figure legend, the reader is referred to the web version of this article.)

0.02 m in both the x and y directions. The beamforming map at 2 kHz is shown in Fig. 22(a). The resulting 95 percent confidence intervals of the integrated DAS levels versus frequency have been plotted in Fig. 22(b) for a frequency range of 1 to 10 kHz. In this figure, the uncertainties for the CSM are calculated for an effective number of blocks of 498 for testing and 1000 for calibration, the uncertainties for individual microphone sensitivities and phases are set to 15 percent and 15°, respectively, the temperature uncertainty is set to 1 percent for testing and 0.1 percent for calibration, the microphone location uncertainties in all the x, y and z directions are set to 10 mm, and the array broadband distance uncertainty is set to 2.5 percent (10 mm standard deviation in microphone locations corresponds to dimensionless perturbations of 0.029

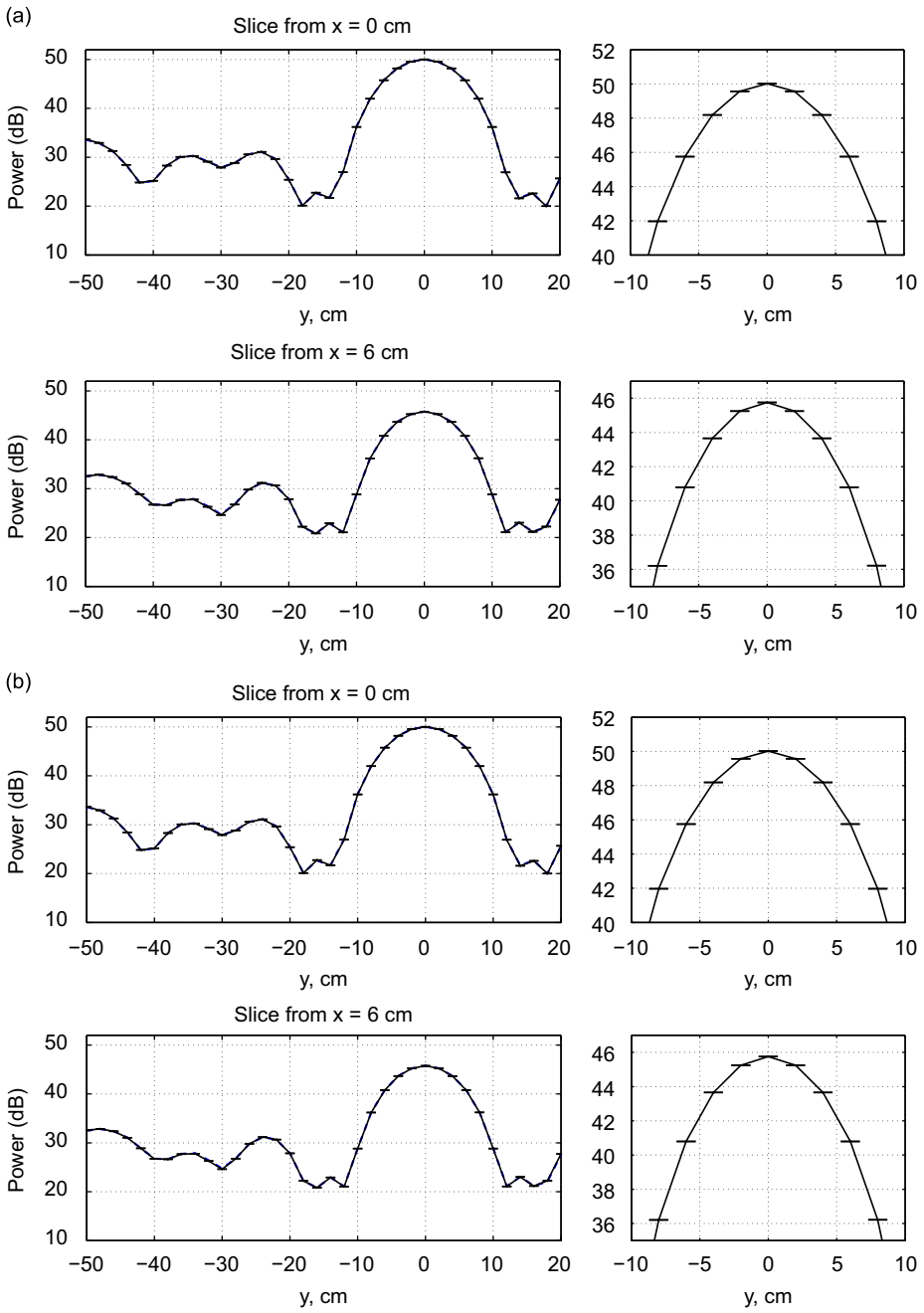

Fig. 19. The 95 percent confidence intervals of the DAS power estimates when the individual microphone phases are perturbed. Two slices from the beamforming image at $x = 0$ and 6 cm are considered. The relative input uncertainties are (a) 1°, and (b) 10°. The black solid line and the blue dashed line indicate the mean values and the nominal values, respectively. A zoomed in view of the main beam region is also provided. The nominal and the mean values are indistinguishable at most y values. Frequency is 5 kHz. (For interpretation of the references to color in this figure legend, the reader is referred to the web version of this article.)

and 0.292 at 1 and 10 kHz, respectively, when normalized by the wavelength). The uncertainties are defined with respect to the assumed nominal values and with experimental data, the "nominal" values might not be identical to the unknown true values. It is observed that the estimated levels are within ± 0.5 dB of the mean value.

As a final case, we analyze the uncertainty in the integrated DAS levels of the NACA 63-215 Mod B airfoil [24,13]. (The details of this aeroacoustic experiment are given by Bahr et al. [13] and hence omitted here due to space concerns.) The beamforming image of the airfoil at 2.5 kHz is shown in Fig. 23(a), where two locations with dominant noise can be identified. Note that in the beamforming map, the scanning region extends from -0.5 to 0.5 m in the x direction and from

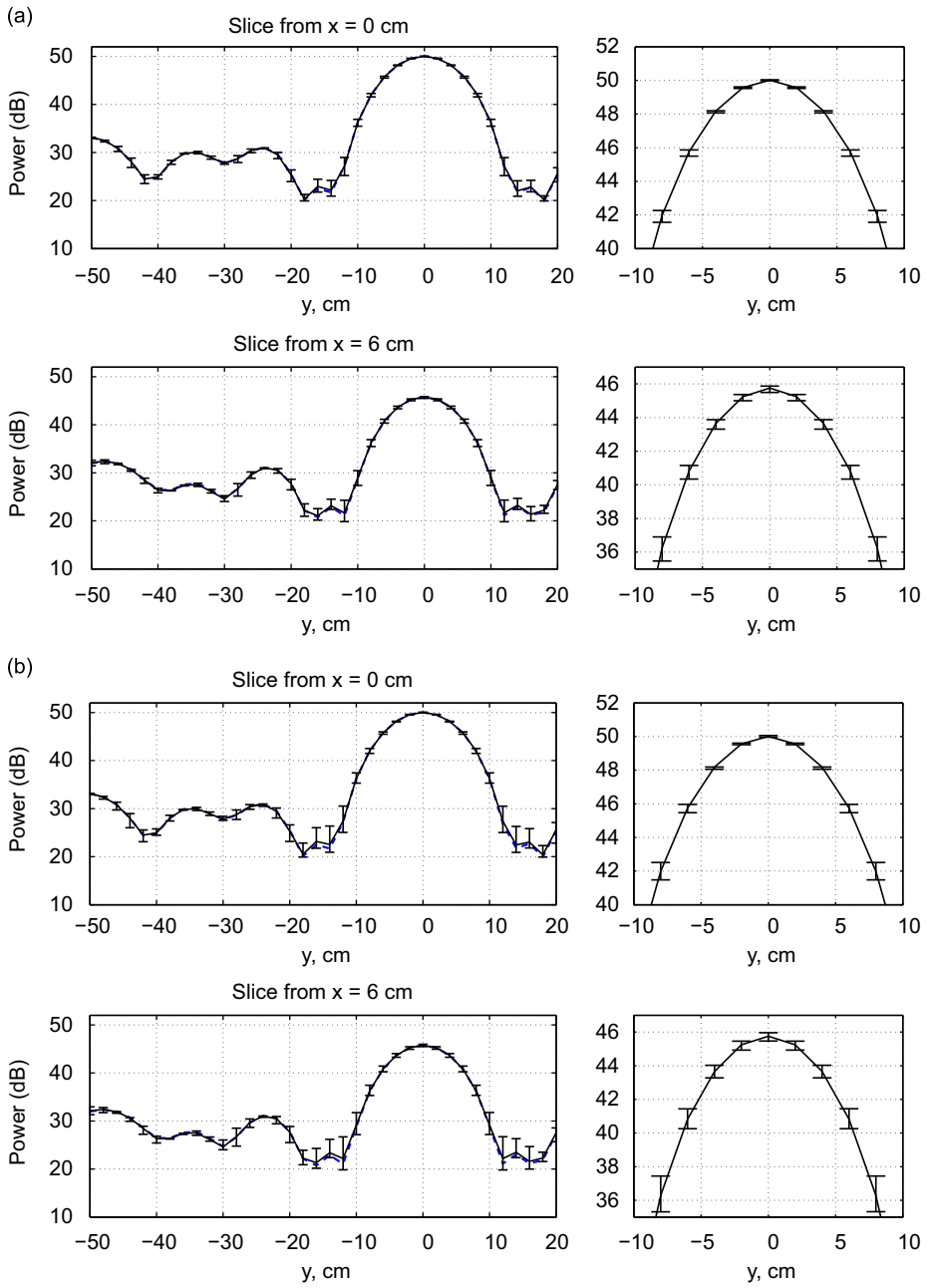

Fig. 20. The 95 percent confidence intervals of the DAS power estimates when the temperature is perturbed. Two slices from the beamforming image at $x = 0$ and 6 cm are considered. The relative input uncertainties are (a) 0.1 °C and (b) 3 °C. The black solid line and the blue dashed line indicate the mean values and the nominal values, respectively. A zoomed in view of the main beam region is also provided. The nominal and the mean values are indistinguishable at most y values. Frequency is 5 kHz. (For interpretation of the references to color in this figure legend, the reader is referred to the web version of this article.)

-0.6 to 0.6 m in the y direction with a common resolution of 0.02 m, and the model is at a broadband distance of 1.30 m with respect to the array plane. The Mach number is 0.17. Due to the presence of flow during the airfoil testing, diagonal removal is applied, i.e., the diagonal of $\mathbf{G}$ is removed in the DAS data reduction equation [1,2]. Moreover, shear layer correction has also been employed [1,25]. The data acquisition time was 5 s, sampling frequency was 65,536 Hz and the block length was 2048 samples (frequency resolution of 32 Hz). A Hanning window with 75 percent overlap has been employed leading to 331 effective averages [13]. The resulting uncertainties in the integrated levels are shown in Fig. 23(b) where the input uncertainties are set to the same values used in the previous example (10 mm standard deviation in microphone locations corresponds to dimensionless perturbations of 0.022 and 0.073 at 0.75 and 2.5 kHz, respectively,

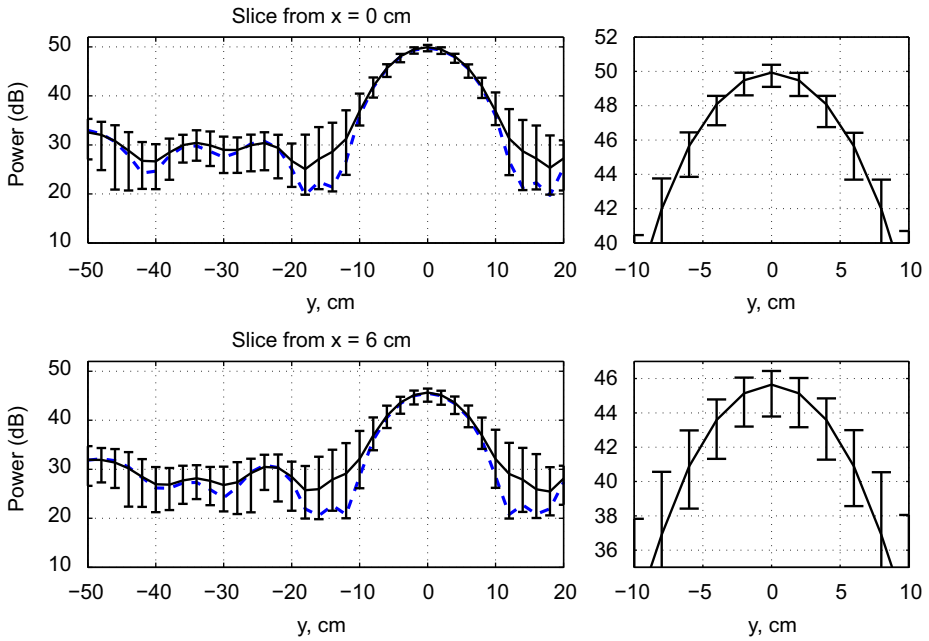

Fig. 21. The 95 percent confidence intervals of the DAS power estimates when all the input variables are perturbed. See the text for specific perturbation values. Two slices from the beamforming image at $x = 0$ and $x = 6$ cm are considered. The black solid line and the blue dashed line indicate the mean values and the nominal values, respectively. A zoomed in view of the main beam region is also provided. The nominal and the mean values are indistinguishable at most y values. Frequency is 5 kHz. (For interpretation of the references to color in this figure legend, the reader is referred to the web version of this article.)

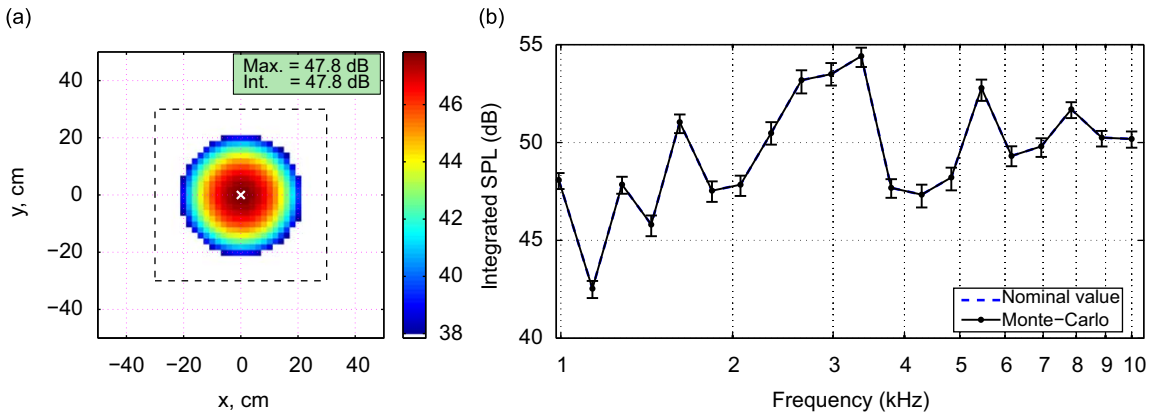

Fig. 22. (a) The beamforming image at 2 kHz. The integration region is indicated with the dashed square and the true source location is indicated with the "×". The maximum (Max.) and integrated (Int.) levels are indicated on the plot. (b) The 95 percent confidence intervals of the integrated DAS levels versus frequency. See the text for the input uncertainties. The nominal and the mean values are indistinguishable at most of the frequencies.

when normalized by the wavelength). We observe that the estimated levels are within ± 1 dB of the mean values over a frequency range of 0.75–2.5 kHz. (Note that the uncertainties due to shear layer corrections have not been considered.)

6. Conclusions

This paper presented the Monte-Carlo uncertainty analysis of the array calibration technique and the multivariate and Monte-Carlo uncertainty analyses of the DAS beamformer. It was shown that the DAS uncertainty obtained from these two methods are similar when the perturbations are relatively small. However, when the component uncertainties are relatively large, the two methods differ due to the breakdown of the first-order assumption of the multivariate technique. It was also shown that the Monte-Carlo method is simpler to implement and provides more flexibility in terms of analyzing the DAS data reduction equation along with calibration. However, the Monte-Carlo method requires approximately 4 times

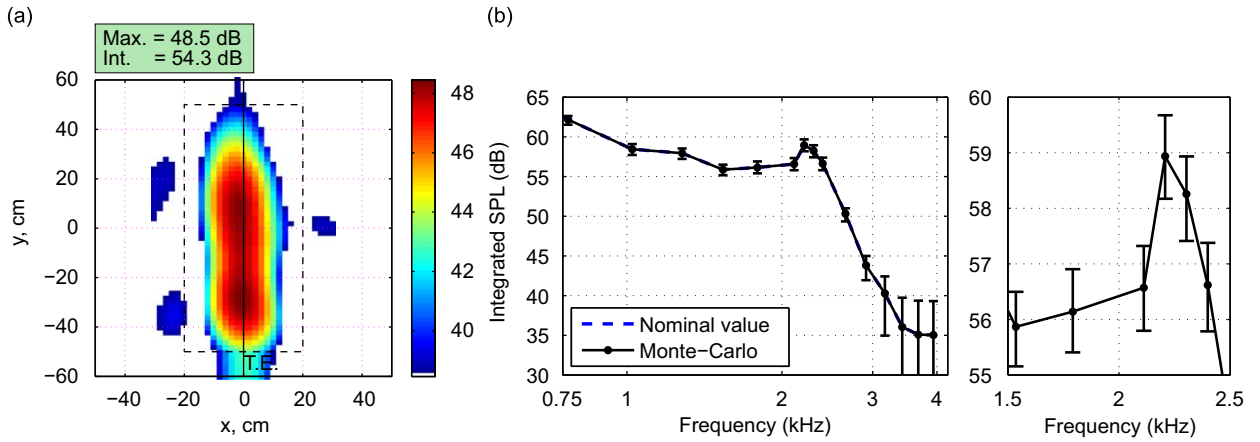

Fig. 23. (a) The beamforming image at 2.5 kHz. The integration region is indicated with the dashed rectangle and the trailing edge (TE) is shown with the solid line. The maximum (Max.) and integrated (Int.) levels are indicated on the plot. (b) The 95 percent confidence intervals of the integrated DAS levels versus frequency. See the text for the input uncertainties. A zoomed in view of the confidence intervals in the frequency range from 1.5 to 2.5 kHz is also provided. The nominal and the mean values are indistinguishable at most of the frequencies.

more computation than the analytic multivariate method for 1000 iterations (and more if the iteration number is increased even further) with the scanning resolutions implemented in this paper.

Using simulations, the calibration procedure was shown to be essential when errors are expected in microphone frequency responses, microphone locations and/or temperature measurements. With calibration, the DAS beamformer was shown to be affected mostly by the uncertainty in the array broadband distance followed by the uncertainties in the CSM and individual microphone sensitivities. In addition to simulations, the uncertainty in the integrated DAS levels of experimental data was also considered. In particular, the 95 percent confidence intervals were found to be around ± 0.5 dB over a frequency range of 1–10 kHz for a single monopole source also used for calibration, whereas with the NACA 63-215 Mod B airfoil model, the 95 percent confidence intervals of the integrated levels were found to be around ± 1 dB over a frequency range of 0.75–2.5 kHz. It should be noted that if the conditions of calibration and testing are significantly different (for instance, if the microphone transfer functions change from calibration to testing), the calibration procedure will be less effective. Therefore, the uncertainties and the confidence intervals provided in this paper could be considered as lower bounds on the errors that will be encountered in practice.

Acknowledgment

This work was supported by the National Aeronautics and Space Administration (NASA) under Grant no. NNX07AO15A.

Appendix A. Jacobian matrix

This appendix derives the closed-form expressions for the Jacobian matrices with respect to all of the input variables in **V** (see Section 4). Note that the Jacobians are evaluated using the nominal values of the input variables.

A.1. Jacobian matrix for the CSM

The derivatives of P_l with respect to the CSM elements are

$$\frac{\partial P_l}{\partial G_{mm}} = \frac{1}{M^2}|\tilde{D}_m|^2\left(\frac{r_{l,m}}{r_{l,0}}\right)^2, \quad m=1,\ldots,M, \tag{A.1}$$

$$\frac{\partial P_l}{\partial C_{mn}} = \frac{2}{M^2}\frac{r_{l,m}r_{l,n}}{r_{l,0}^2}\mathrm{Re}\{\tilde{D}_m\tilde{D}_n^* e^{\mathrm{j}k(r_{l,m}-r_{l,n})}\}, \quad m,n=1,\ldots,M,\ m\neq n, \tag{A.2}$$

and

$$\frac{\partial P_l}{\partial Q_{mn}} = -\frac{2}{M^2}\frac{r_{l,m}r_{l,n}}{r_{l,0}^2}\mathrm{Im}\{\tilde{D}_m\tilde{D}_n^* e^{\mathrm{j}k(r_{l,m}-r_{l,n})}\}, \quad m,n=1,\ldots,M,\ m\neq n, \tag{A.3}$$

where $(\cdot)^*$ denotes the complex conjugate of the argument.

A.2. Jacobian matrix for the calibration factors

The derivative of P_l with respect to D_m can be written as

$$\frac{\partial P_l}{\partial D_m} = \frac{2}{M^2 r_{l,0}^2}\left(r_{l,m}^2 D_m G_{mm} + \mathrm{Re}\left\{r_{l,m}\mathrm{e}^{-\mathrm{j}kr_{l,m}} \sum_{p=1,p\neq m}^{M} r_{l,p}\mathrm{e}^{\mathrm{j}kr_{l,p}}\tilde{D}_p G_{pm}\right\}\right), \quad m=1,\ldots,M. \tag{A.4}$$

The derivative with respect to E_m is obtained by replacing D_m by E_m and the real component by the imaginary component of the argument in Eq. (A.4).

A.3. Jacobian matrix for microphone locations

The derivative of P_l with respect to x_m is given by

$$\frac{\partial P_l}{\partial x_m} = \frac{1}{M^2}\left[|\tilde{D}_m|^2 \frac{\partial}{\partial x_m}\left(\frac{r_{l,m}^2}{r_{l,0}^2}\right) + 2\,\mathrm{Re}\left\{\sum_{p=1,p\neq m}^{M} \tilde{D}_p^* \tilde{D}_m r_{l,p}\mathrm{e}^{-\mathrm{j}kr_{l,p}} \frac{\partial}{\partial x_m}\left(\frac{1}{r_{l,0}^2} r_{l,m}\mathrm{e}^{\mathrm{j}kr_{l,m}}\right)\right\}\right], \tag{A.5}$$

where

$$\frac{\partial}{\partial x_m}(r_{l,m}\mathrm{e}^{\mathrm{j}kr_{l,m}}) = -(\tilde{x}_l - x_m)(1/r_{l,m} + jk)\mathrm{e}^{\mathrm{j}kr_{l,m}}, \tag{A.6}$$

$$\frac{\partial}{\partial x_m}\left(\frac{1}{r_{l,0}^2}\right) = \frac{2(x_l - \overline{x})}{M r_{l,0}^4} \quad \text{and} \quad \frac{\partial r_{l,m}^2}{\partial x_m} = -2(\tilde{x}_l - x_m), \tag{A.7}$$

for $m=1,\ldots,M$. A closed-form expression can be obtained for Eq. (A.5) by using the product rule for differentiation together with Eqs. (A.6) and (A.7). Similar expressions can be obtained for y_m and z_m by replacing $\tilde{x}_l$ with $\tilde{y}_l$ or $\tilde{z}_l$ and x_m with y_m or z_m.

A.4. Jacobian matrix for temperature

The derivative of P_l with respect to temperature can be calculated using

$$\frac{\partial P_l}{\partial T} = \frac{\partial P_l}{\partial k}\frac{\partial k}{\partial T}, \tag{A.8}$$

where

$$\frac{\partial P_l}{\partial k} = -\frac{2}{M^2 r_{l,0}^2}\mathrm{Im}\left\{\sum_{m=1}^{M-1}\sum_{n=m+1}^{M} \tilde{D}_m \tilde{D}_n^* r_{l,m} r_{l,n}(r_{l,m} - r_{l,n})\mathrm{e}^{\mathrm{j}k(r_{l,m}-r_{l,n})} G_{mn}\right\}, \tag{A.9}$$

$$\frac{\partial k}{\partial T} = -\frac{k}{2T_0}, \tag{A.10}$$

and T_0 is the room temperature.

Note that it is difficult to comment on the scaling of the sensitivity coefficients due to the complexity of the corresponding expressions and the high correlation between the input variables. For instance, although it appears that the sensitivity coefficients of the CSM decrease by M^2, the contributions from all the terms ($\mathbf{J}_{\mathrm{CSM}}\mathbf{g}_{\mathrm{CSM}}\mathbf{J}_{\mathrm{CSM}}^{\mathrm{T}}$ in Eq. (26)) will also scale with M^2 and hence the effect of M will be canceled out.

Appendix B. Covariance matrix of the CSM

This appendix derives the covariances between all the real and imaginary components of the $M \times M$ complex symmetric CSM, $\mathbf{G}$ (see Section 4).

Let the pressures measured at microphones m and n be denoted as $p'_m(t)$ and $p'_n(t)$, respectively, where t denotes time. Note that unless otherwise stated, the indices m and n both run from 1 to M. The finite Fourier transforms of $p'_m(t)$ and $p'_n(t)$ are then defined as [19]

$$y_m(f) = \int_0^{\mathrm{T}} p'_m(t)\mathrm{e}^{-\mathrm{j}2\pi ft}\,\mathrm{d}t = y_{m,R}(f) - jy_{m,I}(f)$$

and

$$y_n(f) = \int_0^{\mathrm{T}} p'_n(t)\mathrm{e}^{-\mathrm{j}2\pi ft}\,\mathrm{d}t = y_{n,R}(f) - jy_{n,I}(f), \tag{B.1}$$

where $y_{m,R}(f)$ and $y_{m,I}(f)$ denote the real and imaginary parts of $y_m(f)$, respectively, (similarly for $y_n(f)$) and $T=H/f_s$ is the finite block length in time. The raw estimate for the cross-spectrum is then given by [19]

$$G_{mn}(f_h)=\frac{2}{T}y_m(f_h)y_n^*(f_h),\quad h=0,1,\ldots,H/2. \tag{B.2}$$

Note that when $p'_m(t)$ and $p'_n(t)$ are assumed to be normally distributed with zero mean, so will be $y_m(f)$ and $y_n(f)$. The frequency variable f is omitted in the rest for notational simplicity. From Eqs. (B.1) and (B.2) we obtain [19]

$$G_{mm}=\frac{2}{T}(y_{m,R}^2+y_{m,I}^2),\quad G_{nn}=\frac{2}{T}(y_{n,R}^2+y_{n,I}^2), \tag{B.3}$$

and

$$C_{mn}=\frac{2}{T}(y_{m,R}y_{n,R}+y_{m,I}y_{n,I}),\quad Q_{mn}=\frac{2}{T}(y_{m,R}y_{n,I}-y_{m,I}y_{n,R}). \tag{B.4}$$

Moreover, from Eq. (B.1) evaluated at $f=f_0,f_1,\ldots,f_{H/2}$, or equivalently, at $f=0,1/T,\ldots,H/(2T)$, we obtain [19]

$$E[y_{m,R}y_{m,I}]=E[y_{n,R}y_{n,I}]=0,\quad E[y_{m,R}^2]=E[y_{m,I}^2]=\frac{T}{4}G_{mm},\quad E[y_{n,R}^2]=E[y_{n,I}^2]=\frac{T}{4}G_{nn} \tag{B.5}$$

and

$$E[y_{m,R}y_{n,R}]=E[y_{m,I}y_{n,I}]=\frac{T}{4}C_{mn},\quad E[y_{m,R}y_{n,I}]=-E[y_{m,I}y_{n,R}]=\frac{T}{4}Q_{mn}. \tag{B.6}$$

In order to compute the covariance between C_{mn} and Q_{pq}, we need to find

$$\begin{aligned}E[C_{mn}Q_{pq}]&=\frac{4}{T^2}E[(y_{m,R}y_{n,R}+y_{m,I}y_{n,I})(y_{p,R}y_{q,I}-y_{p,I}y_{q,R})]\\&=\frac{4}{T^2}(E[y_{m,R}y_{n,R}y_{p,R}y_{q,I}]-E[y_{m,R}y_{n,R}y_{p,I}y_{q,R}]+E[y_{m,I}y_{n,I}y_{p,R}y_{q,I}]-E[y_{m,I}y_{n,I}y_{p,I}y_{q,R}])\\&=C_{mn}Q_{pq}+\frac{1}{2}(C_{mp}Q_{nq}+Q_{mq}C_{np}-Q_{mp}C_{nq}-C_{mq}Q_{np}),\end{aligned} \tag{B.7}$$

where we have used the fact that for any four Gaussian variables a_1, a_2, a_3, a_4 with zero mean values [19]

$$E[a_1,a_2,a_3,a_4]=E[a_1,a_2]E[a_3,a_4]+E[a_1,a_3]E[a_2,a_4]+E[a_1,a_4]E[a_2,a_3]. \tag{B.8}$$

Since $E[G_{mm}]=G_{mm}$, $E[G_{nn}]=G_{nn}$, $E[C_{mn}]=C_{mn}$ and $E[Q_{pq}]=Q_{pq}$ (see Eqs. (B.3)–(B.6)), it follows that

$$\mathrm{Cov}(C_{mn},Q_{pq})=\tfrac{1}{2}(C_{mp}Q_{nq}+Q_{mq}C_{np}-Q_{mp}C_{nq}-C_{mq}Q_{np}),\quad m,n,p,q=1,\ldots,M. \tag{B.9}$$

The other covariance formulas listed in Table 2 can be obtained in a similar manner.

Appendix C. Generating Gaussian random variables with a given covariance matrix

This appendix provides a short description on how Gaussian random variables with a given covariance matrix can be generated (see Section 4).

To generate Gaussian random vectors with zero mean and covariance matrix $\boldsymbol{\Sigma}$, we first generate an i.i.d. Gaussian random vector with zero mean and unit variance. Denoting this random vector with $\boldsymbol{\eta}$, $\boldsymbol{\Lambda}\boldsymbol{\eta}$ will yield a Gaussian random vector with covariance matrix $\boldsymbol{\Sigma}$ and zero mean provided that $\boldsymbol{\Lambda}\boldsymbol{\Lambda}^{\mathrm{H}}=\boldsymbol{\Sigma}$. $\boldsymbol{\Lambda}$ can be obtained from the Cholesky decomposition of $\boldsymbol{\Sigma}$ [26].

Let the number of Monte-Carlo trials be denoted by N_{trial}. We recommended that N_{trial} perturbation vectors be generated simultaneously before implementing the Monte-Carlo analysis rather than generating a single perturbation vector at each Monte-Carlo iteration (i.e., N_{trial} times) since calculating $\boldsymbol{\Lambda}$ can be a time-consuming process.

Appendix D. Number of Monte-Carlo iterations

This appendix analyzes the effect of the number of Monte-Carlo iterations on the uncertainty levels. First, consider the example described in Section 5.3.2, where the x, y and z components of the microphone locations were perturbed using i.i.d. Gaussian random variables with zero means and standard deviations of $\sigma_{\mathrm{Locs}}=10$ mm (see Fig. 9). Fig. 24 shows the uncertainty profile plots obtained by using 1000 (see Fig. 9) and 100,000 Monte-Carlo iterations superimposed. It is observed that the two uncertainty plots are indistinguishable at almost all of the y values with the maximum deviation being less than 0.08 dB, which is practically insignificant. Note that for this particular example, the computation times on a personal computer with 2.53 GHz processor speed and 3 GB random access memory were approximately 6 min and 10 h, respectively, for 1000 and 100,000 Monte-Carlo iterations. Using 100,000 Monte-Carlo iterations therefore seems both unnecessary and computationally expensive, especially when integrated DAS level uncertainties are desirable as in our examples. Table 3 lists the mean value, and the lower and upper bounds of the 95 percent confidence interval for the grid point located at the center of the scanning region, i.e., at $(x,y)=(0,0)$ m, obtained by using 1000 and 100,000 Monte-Carlo

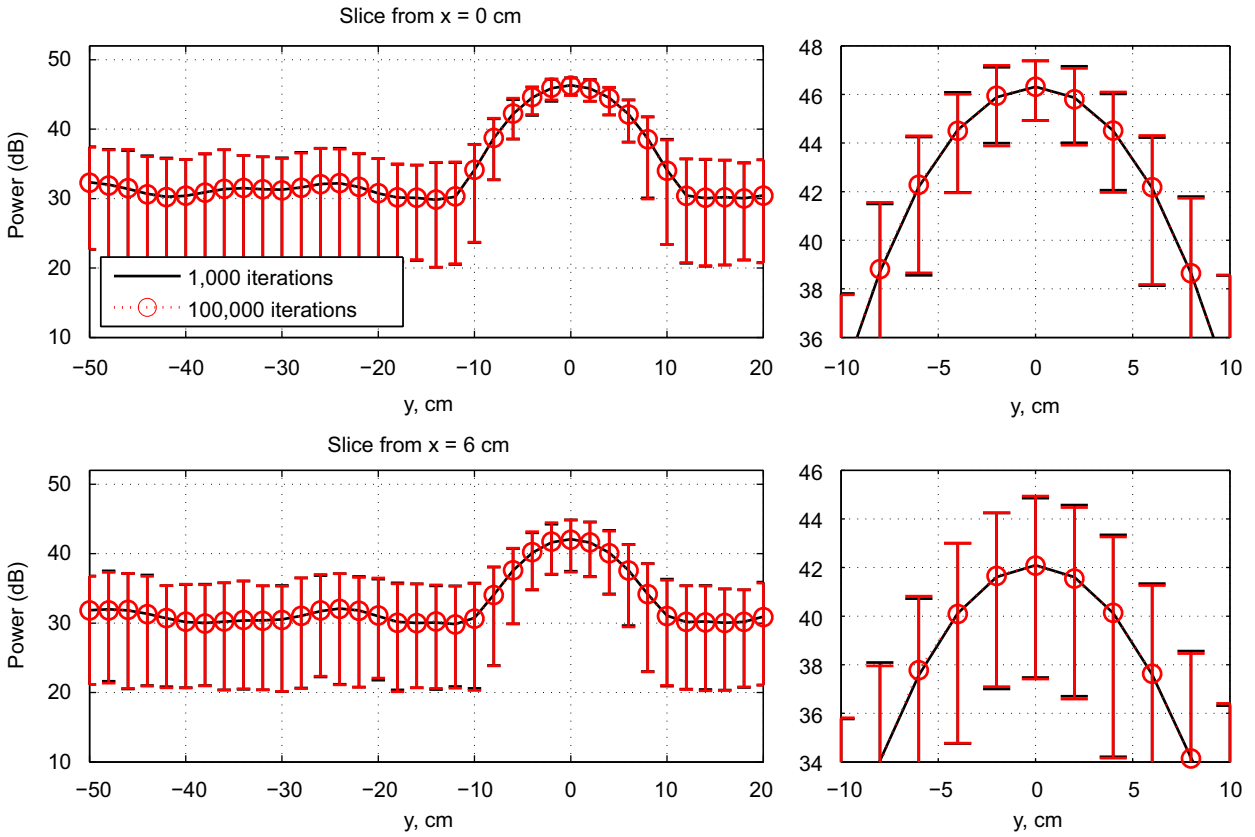

Fig. 24. Profile plots of the mean and the 95 percent confidence intervals when microphone locations are perturbed with a standard deviation of 10 mm. The results obtained by using 1000 and 100,000 Monte-Carlo iterations are shown superimposed. The two plots are indistinguishable at most of the y values.

Table 3
95 percent confidence intervals (dB) obtained by using 1000 and 100,000 Monte-Carlo iterations in 10 sets of trials.

Trial	Lower bound		Mean value		Upper bound	
	1000	100,000	1000	100,000	1000	100,000
#1	44.98	44.98	46.48	46.48	47.57	47.57
#2	44.97	44.98	46.48	46.48	47.57	47.57
#3	44.98	44.98	46.48	46.48	47.57	47.57
#4	44.98	44.98	46.48	46.48	47.58	47.57
#5	44.98	44.98	46.48	46.48	47.57	47.57
#6	44.98	44.98	46.47	46.48	47.57	47.57
#7	44.97	44.98	46.48	46.48	47.57	47.57
#8	44.98	44.98	46.48	46.48	47.57	47.57
#9	44.98	44.98	46.48	46.48	47.56	47.57
#10	44.98	44.98	46.48	46.48	47.57	47.57

iterations. In Table 3, 10 independent sets of trials (with each trial consisting of 1000 or 100,000 Monte-Carlo iterations to compute the confidence interval and mean) have been conducted and only two decimal points are considered as smaller deviations in dB are practically irrelevant. It is again observed that using 1000 Monte-Carlo iterations suffices.

Finally, consider the uncertainty in the DAS integrated levels, in particular the single speaker experimental setup described in Section 5.3.3 (see Fig. 22). In this case, 1000 and 10,000 Monte-Carlo iterations are considered due to the increased computation time. The uncertainty levels in the frequency range from 1 to 10 kHz are shown in Fig. 25. It is observed that using 1000 or 10,000 Monte-Carlo iterations yields nearly identical results.

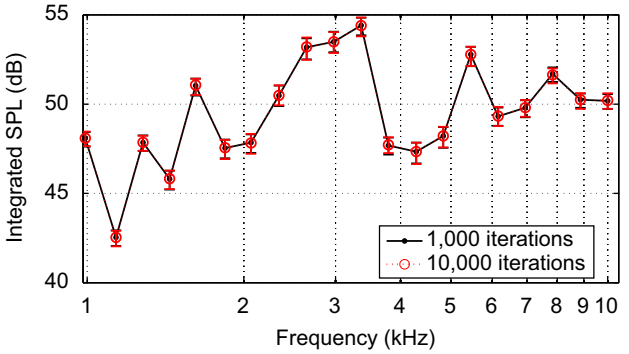

Fig. 25. The 95 percent confidence intervals of the integrated DAS levels versus frequency. The results obtained by using 1000 and 10,000 Monte-Carlo iterations are shown superimposed. The two plots are indistinguishable at most of the frequencies.

Appendix E. More on microphone location errors

This appendix elaborates on the bias observed in the DAS power estimates when the microphone locations are perturbed (see Section 5.3.2).

Assume that there is only a single source present and that there is no contaminating noise. Moreover assume that only the microphone locations are perturbed. Consequently (see Eq. (7)),

$$\mathbf{G} = P_0 \mathbf{a}\mathbf{a}^{\mathrm{H}}, \tag{E.1}$$

where P_0 is the power of the source and $\mathbf{a}$ is the steering vector corresponding to the source, i.e., $\mathbf{a} = [\mathrm{e}^{-\mathrm{j}kr_{0,1}}/r_{0,1}, \ldots, \mathrm{e}^{-\mathrm{j}kr_{0,M}}/r_{0,M}]^{\mathrm{T}}$, with $r_{0,m}$ denoting the distance between the m th microphone and the source location. When the microphone locations are perturbed, the distance between the m th microphone and the source location becomes $r_{0,m}+\delta r_m$, where δr_m denotes the perturbation and it can be negative or positive. The perturbed DAS estimate of the source power is then (by omitting calibration errors in Eq. (8))

$$\hat{P}_0 = \frac{1}{M^2} \tilde{\mathbf{a}}_p^{\mathrm{H}} \mathbf{G} \tilde{\mathbf{a}}_p, \tag{E.2}$$

where $\tilde{\mathbf{a}}_p$ is the perturbed version of Eq. (5) and is defined as

$$\tilde{\mathbf{a}}_p = \frac{1}{r_{0,0}} [(r_{0,1}+\delta r_1)\mathrm{e}^{-\mathrm{j}k(r_{0,1}+\delta r_1)}, \ldots, (r_{0,M}+\delta r_M)\mathrm{e}^{-\mathrm{j}k(r_{0,M}+\delta r_M)}]^{\mathrm{T}}. \tag{E.3}$$

Note that $r_{0,0}$ (the distance between the source and the array center) is not going to be affected much by the perturbations since the array center will remain approximately at the same location when the microphone locations are perturbed with i.i.d. Gaussian random variables with zero mean values. Therefore,

$$\hat{P}_0 = \left| \frac{1}{M} \sum_{m=1}^{M} \left(1+\frac{\delta r_m}{r_{0,m}}\right) \mathrm{e}^{\mathrm{j}k\delta r_m} \right|^2 \tilde{P}_0, \tag{E.4}$$

where $\tilde{P}_0 = P_0/r_{0,0}^2$ is the source power at the array center. Note that when the microphone locations are not perturbed, $\delta r_m = 0$, $m = 1, \ldots, M$, and hence $\hat{P}_0 = \tilde{P}_0$. However, when $\delta r_m \neq 0$, since f is relatively large and the perturbations appear on the phase terms, even small perturbations can affect the overall result. Using the Cauchy–Schwarz inequality gives [27]

$$\left| \frac{1}{M} \sum_{m=1}^{M} \left(1+\frac{\delta r_m}{r_{0,m}}\right) \mathrm{e}^{\mathrm{j}k\delta r_m} \right|^2 \leq 1 + \frac{1}{M} \sum_{m=1}^{M} \frac{2\delta r_m}{r_{0,m}} + \frac{1}{M} \sum_{m=1}^{M} \left(\frac{\delta r_m}{r_{0,m}}\right)^2 \approx 1,$$

where since $\delta r_m \ll r_{0,m}$, the second and third terms have been neglected in the last equality. So, we can approximately claim that $\hat{P}_0 \leq \tilde{P}_0$. We plot $(1+\delta r_m/r_{0,m})\mathrm{e}^{\mathrm{j}k\delta r_m}$, $m = 1, \ldots, M$, for a single Monte-Carlo trial in Fig. 26, where the standard deviation of the perturbation δr_m is chosen to be 1 and 10 mm. We observe that as $f\delta r_m$ gets larger, the phase $k\delta r_m = 2\pi f/c\delta r_m$ starts to deviate from the nominal value of 0°, whereas the amplitude is always around 1 regardless of f since $(1+\delta r_m/r_{0,m}) \approx 1$. Therefore, we conclude that for relatively large $f\delta r_{0,m}$, the average of the samples (marked with a cross in the plots) will have amplitude much smaller than 1 which means that the average squared, i.e., $\hat{P}_0/\tilde{P}_0$, will be even smaller.

Another rather simple argument is that since the non-perturbed $\tilde{\mathbf{a}}_l$ are designed so as to maximize the beamforming output for the l th scanning point, when the locations are perturbed, the mismatch between $\tilde{\mathbf{a}}_l$ and $\mathbf{a}_l$ will result in equal or smaller power estimates than the true power. Therefore, this will create a negative bias in the power estimates.

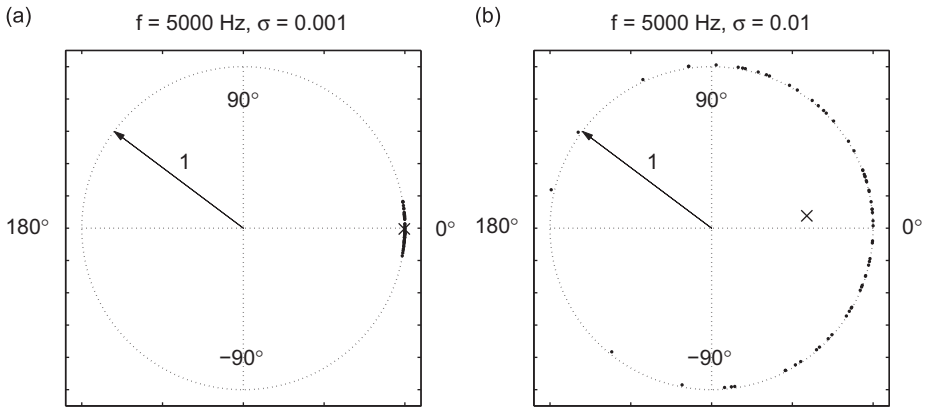

Fig. 26. The polar plot of $(1+\delta r_m/r_{0,m})e^{jk\delta r_m}$, $m=1,\ldots,M$, at one Monte-Carlo trial, where the standard deviation of the perturbation δr_m is chosen to be (a) 1 mm and (b) 10 mm. f=5 kHz and z=1.48 m as usual. The cross-marks indicate the averages of the M values in each plot.

References

[1] W.M. Humphreys, T.F. Brooks, W.W. Hunter, K.R. Meadows, Design and use of microphone directional arrays for aeroacoustic measurements, *4th AIAA/CEAS Aeroacoustics Conference*, AIAA-98-0471, Reno, NV, 1998.
[2] R.P. Dougherty, in: T.J. Mueller (Ed.), *Beamforming in Acoustic Testing, Aeroacoustic Measurements*, Springer, Berlin, 2002, pp. 63–97.
[3] K.R. Meadows, T.F. Brooks, W.M. Humphreys Jr., W.W. Hunter, C.H. Gerhold, Aeroacoustic measurements of a wing-flap configuration, *3rd AIAA/CEAS Aeroacoustics Conference*, AIAA Paper 97-1595, Atlanta, GA, 1997.
[4] R.P. Dougherty, Advanced time-domain beamforming techniques, *10th AIAA/CEAS Aeroacoustics Conference*, AIAA-2004-2955, Manchester, UK, 2004.
[5] T.F. Brooks, W.M. Humphreys, A deconvolution approach for the mapping of acoustic sources (DAMAS) determined from phased microphone arrays, *10th AIAA/CEAS Aeroacoustics Conference*, AIAA-2004-2954, Manchester, UK, 2004.
[6] R.P. Dougherty, Extensions of DAMAS and benefits and limitations of deconvolution in beamforming, *11th AIAA/CEAS Aeroacoustics Conference*, AIAA-2005-2961, Monterey, CA, 2005.
[7] T. Yardibi, J. Li, P. Stoica, L.N. Cattafesta, Sparsity constrained deconvolution approaches for acoustic source mapping, *14th AIAA/CEAS Aeroacoustics Conference*, AIAA-2008-2957, British Columbia, Canada, 2008.
[8] T. Yardibi, J. Li, P. Stoica, L.N. Cattafesta, Sparsity constrained deconvolution approaches for acoustic source mapping, *The Journal of the Acoustical Society of America* 123 (5) (2008) 2631–2642.
[9] P. Sijtsma, Clean based on spatial source coherence, *International Journal of Aeroacoustics* 6 (4) (2007) 357–374.
[10] H.W. Coleman, W.G. Steele, *Experimentation and Uncertainty Analysis for Engineers*, Wiley, NY, 1998.
[11] T. Schultz, M. Sheplak, L.N. Cattafesta, Uncertainty analysis of the two-microphone method, *Journal of Sound and Vibration* 304 (1–2) (2007) 91–109.
[12] P. Castellini, M. Martarelli, Acoustic beamforming: analysis of uncertainty and metrological performances, *Mechanical Systems and Signal Processing* 22 (3) (2008) 672–692.
[13] C. Bahr, T. Yardibi, F. Liu, L.N. Cattafesta, An analysis of different measurement techniques for airfoil trailing edge noise, *14th AIAA/CEAS Aeroacoustics Conference*, AIAA-2008-2957, British Columbia, Canada, 2008.
[14] D.T. Blackstock, *Fundamentals of Physical Acoustics*, Wiley, New York, NY, 2000.
[15] D.H. Johnson, D.E. Dudgeon, *Array Signal Processing: Concepts and Techniques*, Prentice-Hall, Englewood Cliffs, NJ, 1993.
[16] B.D. Hall, Calculating measurement uncertainty for complex-valued quantities, *Measurement Science and Technology* 14 (2003) 368–375.
[17] B.D. Hall, On the propagation of uncertainty in complex-valued quantities, *Metrologia* 41 (2004) 173–177.
[18] T. Schultz, M. Sheplak, L.N. Cattafesta, Application of multivariate uncertainty analysis to frequency response function estimates, *Journal of Sound and Vibration* 305 (1–2) (2007) 116–133.
[19] J.S. Bendat, A.G. Piersol, *Random Data: Analysis and Measurement Procedures*, Wiley, New York, 2000.
[20] J.R. Underbrink, *Practical Considerations in Array Design for Passive Broad-Band Source Mapping Applications*, The Pennsylvania State University, State College, PA, 1995.
[21] J.R. Underbrink, T.J. Mueller (Eds.), *Aeroacoustic Phased Array Testing in Low Speed Wind Tunnels, Aeroacoustic Measurements*, Springer, Berlin, 2002, pp. 99–217.
[22] T.F. Brooks, W.M. Humphreys Jr., Effect of directional array size on the measurement of airframe noise components, *5th AIAA/CEAS Aeroacoustics Conference*, AIAA-99-1958, Bellevue, WA, 1999.
[23] S. Oerlemans, L. Broersma, P. Sijtsma, Quantification of airframe noise using microphone arrays in open and closed wind tunnels, *International Journal of Aeroacoustics* 6 (4) (2007) 309–333.
[24] F.V. Hutcheson, T.F. Brooks, Measurement of trailing edge noise using directional array and coherent output power methods, *International Journal of Aeroacoustics* 1 (4) (2002) 329–354.
[25] R.K. Amiet, Refraction of sound by a shear layer, *Journal of Sound and Vibration* 58 (3) (1978) 467–482.
[26] G.H. Golub, C.F. Van Loan, *Matrix Computations*, third ed., The John Hopkins University Press, Baltimore, MD, 1996.
[27] W. Rudin, *Principles of Mathematical Analysis*, third ed., McGraw-Hill, New York, 1976.